

AKARI INFRARED CAMERA SURVEY OF THE LARGE MAGELLANIC CLOUD. I. POINT-SOURCE CATALOG

DAISUKE KATO^{1,2,3}, YOSHIFUSA ITA⁴, TAKASHI ONAKA¹, TOSHIHIKO TANABÉ⁵, TAKASHI SHIMONISHI^{1,10}, ITSUKI SAKON¹,
 HIDEHIRO KANEDA⁶, AKIKO KAWAMURA⁷, TAKEHIKO WADA², FUMIHIKO USUI², BON-CHUL KOO⁸,
 MIKAKO MATSUURA⁹, AND HIDENORI TAKAHASHI⁵

¹ Department of Astronomy, Graduate School of Science, The University of Tokyo, 7-3-1 Hongo, Bunkyo-ku, Tokyo 113-0033, Japan;
kato@ir.isas.jaxa.jp, onaka@astron.s.u-tokyo.ac.jp

² Institute of Space and Astronautical Science, Japan Aerospace Exploration Agency, 3-1-1 Yoshino-dai, Chuo-ku, Sagami-hara, Kanagawa 252-5210, Japan

³ Center for Low Carbon Society Strategy, Japan Science and Technology Agency, 7 Goban-cho, Chiyoda-ku, Tokyo 102-0076, Japan

⁴ Astronomical Institute, Tohoku University, 6-3 Aramaki, Aoba-ku, Sendai, Miyagi 980-8578, Japan

⁵ Institute of Astronomy, School of Science, The University of Tokyo, 2-21-1 Osawa, Mitaka, Tokyo 181-0015, Japan

⁶ Graduate School of Science, Nagoya University, Chikusa-ku, Nagoya 464-8602, Japan

⁷ National Astronomical Observatory of Japan, 2-21-1 Osawa, Mitaka, Tokyo 181-8588, Japan

⁸ Department of Physics and Astronomy, Seoul National University, Seoul 151-742, Republic of Korea

⁹ Department of Physics and Astronomy, University College London, Gower Street, London WC1E 6BT, UK

Received 2012 June 29; accepted 2012 September 27; published 2012 November 9

ABSTRACT

We present a near- to mid-infrared point-source catalog of five photometric bands at 3.2, 7, 11, 15, and 24 μm for a 10 deg² area of the Large Magellanic Cloud (LMC) obtained with the Infrared Camera on board the *AKARI* satellite. To cover the survey area the observations were carried out at three separate seasons from 2006 May to June, 2006 October to December, and 2007 March to July. The 10 σ limiting magnitudes of the present survey are 17.9, 13.8, 12.4, 9.9, and 8.6 mag at 3.2, 7, 11, 15, and 24 μm , respectively. The photometric accuracy is estimated to be about 0.1 mag at 3.2 μm and 0.06–0.07 mag in the other bands. The position accuracy is 0'3 at 3.2, 7, and 11 μm and 1'0 at 15 and 24 μm . The sensitivities at 3.2, 7, and 24 μm are roughly comparable to those of the *Spitzer* SAGE LMC point-source catalog, while the *AKARI* catalog provides the data at 11 and 15 μm , covering the mid-infrared spectral range contiguously. Two types of catalog are provided: a Catalog and an Archive. The Archive contains all the detected sources, while the Catalog only includes the sources that have a counterpart in the *Spitzer* SAGE point-source catalog. The Archive contains about 650,000, 140,000, 97,000, 43,000, and 52,000 sources at 3.2, 7, 11, 15, and 24 μm , respectively. Based on the catalog, we discuss the luminosity functions at each band, the color–color diagram, and the color–magnitude diagram using the 3.2, 7, and 11 μm band data. Stars without circumstellar envelopes, dusty C-rich and O-rich stars, young stellar objects, and background galaxies are located at distinct regions in the diagrams, suggesting that the present catalog is useful for the classification of objects toward the LMC.

Key words: catalogs – infrared: galaxies – infrared: stars – Magellanic Clouds – surveys

Online-only material: color figures

1. INTRODUCTION

The Large Magellanic Cloud (LMC) is one of the nearest galaxies. The proximity of the LMC (~ 50 kpc; e.g., Alves 2004) allows us to study individual stars in detail. The mean metallicity of the LMC is also known to be small ($\sim 1/4$) compared with the solar abundance (e.g., Luck et al. 1998), providing us with an ideal place to study formation and evolution of stars in low-metallicity environments.

Individual stars in the LMC have been observed by large area surveys at optical and near-infrared (NIR) wavelengths. Zaritsky et al. (2004) detected about 2.4×10^7 point sources in a *UBVI* survey over a 64 deg² area of the LMC, whereas Kato et al. (2007) observed about 1.5×10^7 point sources with a *JHK_s* survey of a 40 deg² region. At mid-infrared (MIR) wavelengths, the *Midcourse Space Experiment* carried out a survey over a 100 deg² area of the LMC (Egan et al. 2001, 2003) and detected a few thousand sources despite the short integration time and low spatial resolution. Two recent infrared satellites, *Spitzer Space Telescope* (Werner et al. 2004) and *AKARI* (Murakami et al. 2007), provided a capability of deep

mid-infrared observations with better spatial resolution. The *Spitzer* SAGE project (Meixner et al. 2006) carried out a uniform and unbiased imaging survey of a 49 deg² area of the LMC at four photometric bands from 3 to 8 μm of IRAC (Fazio et al. 2004) and three bands at 24, 70, and 160 μm of MIPS (Rieke et al. 2004), to which the SAGE-Spec performed follow-up spectroscopic observations in the MIR and far-infrared (FIR; Kemper et al. 2010; van Loon et al. 2010; Woods et al. 2011). Recently, *Herschel Space Observatory* also made a survey observation over a $8^\circ \times 8.5^\circ$ area of the LMC with spatial resolution higher than *Spitzer* in the FIR (Meixner et al. 2010).

The *AKARI* LMC survey consists of an NIR to MIR imaging and near-infrared spectroscopic survey toward the LMC. The survey aims at a thorough study of the lifecycle of matters and the star formation history of the LMC on a galactic scale owing to its wide spatial coverage and high sensitivities over the wide spectral range (Ita et al. 2008). The sensitivities are comparable to those of the *Spitzer* SAGE survey and the *AKARI* survey covers the MIR spectral range contiguously, which fills the gap between the *Spitzer*/IRAC and MIPS bands. In addition to the dedicated survey observations, the entire LMC was observed as part of the all-sky survey at six bands from the MIR to the FIR (Ishihara et al. 2010; Kawada et al. 2007). The MIR

¹⁰ Present address: Department of Earth and Planetary Sciences, Graduate School of Science, Kobe University, Nada Kobe 657-8501, Japan.

point-source catalog at 9 and 18 μm and the FIR point-source catalog at 65, 90, 140, and 160 μm have been produced from the all-sky survey observations and released to the public (Ishihara et al. 2010; Yamamura et al. 2010). These *AKARI* observations provide 11 band data of the LMC from the NIR to the FIR, which give us a unique and useful database for the study of the LMC.

A brief description of the *AKARI* LMC survey and early results have been given in Ita et al. (2008) based on a preliminary version of the catalog. The catalog has been revised by improving the data reduction procedure, which increases the reliability and accuracy of the photometric results. In this paper, we describe the point-source catalog from the imaging survey of the LMC from the NIR to the MIR using the latest version of the data reduction process, which will be released to the public. We outline the *AKARI* LMC survey observations in Section 2, the data reduction procedures in Section 3, and the structure of the catalog in Section 4. The general characteristics of the catalog are presented in Section 5, and the properties of the sources in the catalog are discussed in Section 6. A summary is given in Section 7.

2. OBSERVATIONS

The *AKARI* telescope has an effective aperture of 685 mm (Kaneda et al. 2007) and the whole telescope system including the focal-plane instruments was cooled by liquid helium and onboard mechanical coolers. The *AKARI* spacecraft was brought into a Sun-synchronous polar orbit at an altitude of 700 km along the twilight zone, similar to that of the *IRAS* satellite. The LMC is located near the south ecliptic pole, where the polar orbit has high visibility. Taking this advantage, we observed the main part of the LMC contiguously.

The *AKARI* LMC survey was carried out with the Infrared Camera (IRC; Onaka et al. 2007) in the pointing observation mode (Murakami et al. 2007). It has three independent channels: NIR (1.8–5.5 μm), MIR-S (4.6–13.4 μm), and MIR-L (12.6–26.5 μm). Each channel has a wide field of view (FoV) of about $10' \times 10'$ and is equipped with three imaging filters and two dispersion elements, which can be switched during a pointing observation. Of these, we use five imaging filters at 3.2 (N3), 7 (S7), 11 (S11), 15 (L15), and 24 μm (L24), and the prism for slitless spectroscopy in 2–5 μm (NP) of a spectral resolution of $\lambda/\Delta\lambda \sim 20$ (Ohya et al. 2007), where the symbol in parentheses indicates the filter designation. The imaging bands cover the spectral range from 5 to 26 μm contiguously and the S11 and L15 bands fill the gap in the wavelength coverage between the IRAC and MIPS on board *Spitzer*. The present photometric catalog is produced from the imaging data. Part of the data taken in the slitless spectroscopic mode are reported in Shimonishi et al. (2008). The data reduction and the extracted spectra with the slitless spectroscopic mode will be given separately (Shimonishi et al. 2012).

We use the *AKARI* IRC AOT02 observation template with a special option (using the prism instead of the N4 filter) prepared for the LMC survey. The template is designed to take images with two filters in each channel at three dithered sky positions in a pointing observation. At each position, both short- and long-exposure data are taken. The net integration times for a long-exposure image are typically 133, 147, and 147 s for the NIR, MIR-S, and MIR-L channels, respectively, and that for a short-exposure image is 14.0, 1.75, and 1.75 s, respectively (Table 1). The long-to-short exposure time ratios of a pointing observation are 9.5, 28, and 28 for the NIR, MIR-S, and MIR-L

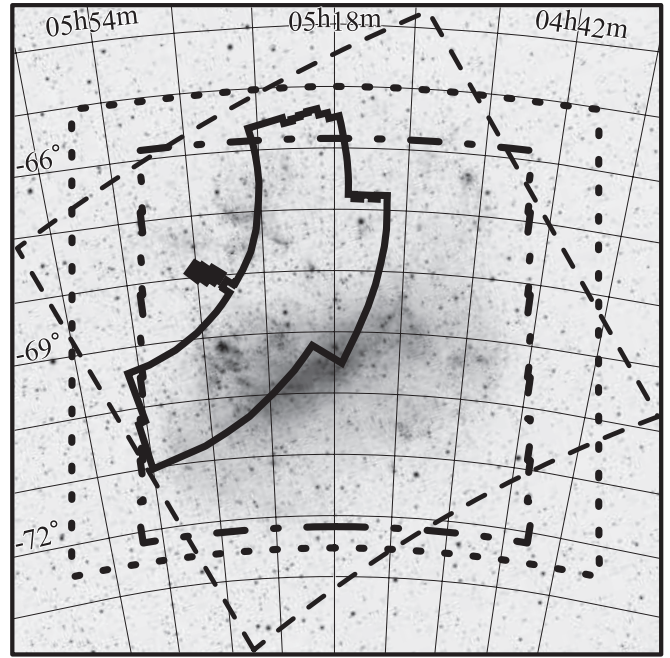


Figure 1. Observed area of the *AKARI* IRC survey (solid outline) overlaid on the photographic image kindly provided by Motonori Kamiya. The dashed outline indicates the coverage of the *Spitzer* SAGE survey ($7^\circ \times 7^\circ$; Meixner et al. 2006), the dash-dotted outline shows the coverage of the IRSF/SIRIUS near-infrared survey (6.3×6.3 ; Kato et al. 2007), and the dotted outline represents the coverage of the Magellanic Clouds optical photometric survey (8.5×7.5 ; Zaritsky et al. 2004).

channels, respectively, which increases the dynamic range of the observations (see Section 3.5.2).

The NIR and MIR-S channels share the same FoV by means of the beam splitter, and thus N3, NP, S7, and S11 images are taken at the same region simultaneously. L15 and L24 images of the same region are taken at a different pointing observation since their FoV is located $20'$ away from that of the NIR/MIR-S in the direction perpendicular to the *AKARI* orbit (Onaka et al. 2007). The FoV of the *AKARI* telescope moves along the ecliptic meridian in the twilight zone, which changes its direction with the Earth's yearly orbit. Therefore, the telescope can observe a given celestial position twice a year. The position of the MIR-L channel relative to the NIR and MIR-S channels is flipped in projection on the sky at a season separated by half a year because the satellite moves in the opposite direction. Taking account of the change in the projection direction, we optimize the target positions to maximize the area observed by all the three IRC channels with the overlapping region of 1/5 for each image.

Observations were carried out in three separate seasons, from 2006 May 6 to June 8, from 2006 October 2 to December 31, and from 2007 March 24 to July 2. Over 600 pointing observations were devoted to this project, yielding imaging and spectroscopic maps of about a 10 deg^2 area of the main part of the LMC. Figure 1 shows the area where the *AKARI* survey was carried out together with the areas of other surveys.

3. DATA REDUCTION AND COMPILATION OF THE POINT-SOURCE CATALOG

3.1. Imaging Data Reduction

Standard procedures for the reduction of imaging data obtained with infrared arrays, dark subtraction, flat fielding, and image co-addition, are performed in the IRC data reduction

Table 1
Observation Parameters

Properties	IRC Bands					
	NP	N3	S7	S11	L15	L24
Channel	NIR	NIR	MIR-S	MIR-S	MIR-L	MIR-L
Bandpass (μm)	1.8–5.5	2.7–3.8	5.9–8.4	8.5–13.1	12.6–19.4	20.3–26.5
Reference wavelength (μm)	...	3.2	7.0	11.0	15.0	24.0
Pixel field of view ($''$ pixel $^{-1}$)	...	1.446	2.340	2.340	2.384	2.384
Dispersion (μm pixel $^{-1}$)	0.06 at 3.5 μm
Exposure time: long exposure ^a (s)	133	133	147	147	147	147
Exposure time: short exposure ^a (s)	14.0	14.0	1.75	1.75	1.75	1.75
10 σ detection limit ^b (mJy)	...	0.024	0.226	0.419	1.758	2.921
10 σ detection limit ^b (mag)	...	17.9	13.8	12.4	9.9	8.6
Saturation limit ^{b,c} (mJy)	12500 at 3.5 μm	250	1800	1800	2500	23000
Saturation limit ^{b,c} (mag)	3.6 at 3.5 μm	7.8	4.0	3.3	2.0	−1.1
Zero-magnitude flux density ^d (Jy)	...	343	75.0	38.3	16.0	8.0
Number of sources in Archive	...	720872	141617	97226	42974	52266
Number of sources in Catalog	...	651294	89610	48525	16712	6856

Notes.

^a These are the nominal values. The total exposure time per pixel depends on the co-adding process.

^b For point sources.

^c Numbers are taken from ASTRO-F Observer's Manual version 3.2.2.

^d From Tanabé et al. (2008).

toolkit version 20110304 (Lorente et al. 2008). Since the basic data reduction is carried out in the standard tool kit with the default options, we briefly summarize the procedures below.

1. First the detector nonlinearity is corrected for in each exposure image. Deviations from the ideal linear response are estimated to be smaller than 5% at 12,000, 20,000, and 20,000 ADU for NIR, MIR-S, and MIR-L, respectively, which roughly correspond to the saturation levels of 0.26, 1.9, 1.8, 2.5, and 22 Jy for the short-exposure data at N3, S7, S11, L15, and L24, respectively (see also Table 1).
2. The dark image is subtracted from each image. We use the dark data taken at the beginning of the pointing observation sequence (“pre-dark”) for the MIR-S and MIR-L long-exposure images by averaging three long-exposure data (“self-dark”). For all the short-exposure and NIR long-exposure images, we use the “super-dark” images, which are created by averaging more than 70 “pre-dark” images in the LMC observations and are provided as the default dark data in the IRC toolkit. To correct for the possible time variation between the “super-dark” and the dark image at the time of observation, the signal level of the “super-dark” image is scaled to that of the observed image at the slit mask region before the dark subtraction, assuming that the dark image pattern does not change with time.
3. Signals due to high-energy ionizing particle hits (hereafter cosmic rays) are removed with the task COSMICRAYS in IRAF. Remaining faint cosmic-ray events are removed by median average in step 6.
4. Each image is divided by the flat-field image to correct for the pixel-to-pixel variation in the sensitivity over the arrays. We employ the “super flat-field” images created from images near the North Ecliptic Pole, where the smooth zodiacal emission dominates. We use the MIR-L flat data, in which the effect of the artifacts by internal reflections is corrected (Arimatsu et al. 2011).
5. The aspect ratio of each image is adjusted to 1 to 1 by resampling the image. After the adjustment, the deviation from an ideal grid square is 0.2–0.3 pixel in the NIR

and MIR-S images. In the MIR-L images, the deviation becomes ~ 1 pixel at the edge of the detector. The final pixel scale of the rescaled images is 1 $''$.446, 2 $''$.340, and 2 $''$.384 for the NIR, MIR-S, and MIR-L images, respectively.

6. Images taken at dithered positions are spatially aligned and co-added by taking their median to eliminate any array anomalies, such as bad, dead, or hot pixels, and remaining cosmic-ray events. Images are taken at least at three different positions in a pointing observation in the observation template AOT02.

3.2. Source Detection and Photometry

We perform source detection with the IRAF¹¹/DAOFIND and photometry with the IRAF/DAOPHOT package (Stetson 1987) on co-added images. We develop a procedure for the photometry with the point-spread function (PSF) fitting, which is similar to that used by the *Spitzer* GLIMPSE¹² team (Benjamin et al. 2003). The procedure of the source detection and photometry involves the following steps.

1. DAOFIND is used to extract point-like sources whose fluxes are more than 2σ above the background. The extracted sources include those slightly extended compared with the PSF.
2. The aperture photometry is performed on the extracted sources with an aperture radius of 10.0 pixels for N3 images, and of 3.0 pixels for other band images using the PHOT task in IRAF. The radius of 10.0 pixels at N3 is the same as the one used for the absolute flux calibration (Tanabé et al. 2008). Therefore, we do not apply aperture corrections for the photometry at N3. For the MIR band images, we adopt a smaller aperture than that used in the calibration (7.5 pixels) because of the large background emission in the LMC at the MIR and thus the aperture correction is needed (see step 6).

¹¹ IRAF is distributed by the National Optical Astronomy Observatory, which is operated by the Association of Universities for Research in Astronomy, Inc., under cooperative agreement with the National Science Foundation.

¹² <http://www.astro.wisc.edu/glimpse/>, and see the document “Description of Point Source Photometry Steps Used by GLIMPSE,” by B. L. Babler.

The inner radius of the sky annulus is set as the same as the aperture radius and the width of the sky annulus is set as 5.0 pixels.

3. Bright but unsaturated sources without any other sources within 7 pixels are selected from the results of step 2 to construct the PSF. At least eight of such “good” sources are selected in the N3, S7, and S11 images, and five in the L15 and L24 images.
4. The “good” sources selected in step 3 are used to construct a model PSF for each N3 image since the PSF in the N3 images notably varies from pointing to pointing, possibly due to jitters in the satellite pointing. We use the PSF task in DAOPHOT to choose the best-fitting function by trying several different types of fitting functions in each image.

For the S7, S11, L15, and L24 images, we use the common PSFs constructed in advance for each band, instead of constructing them from each image since the effect of the jitter in the satellite pointing is negligible compared to the size of the PSFs. The common PSFs are constructed from about 10 “good” sources, which are selected from the images taken with the LMC survey and the observations of 47 Tuc (Ita et al. 2007); sources free from diffuse emission are carefully chosen by eye. To construct the common PSFs, the “moffat25,” “lorentz,” “moffat15,” and “gauss” models are applied at S7, S11, L15, and L24, respectively.

5. The PSF-fitting photometry is performed for the extracted sources in step 2 using ALLSTAR in DAOPHOT in an iterative manner. After the first ALLSTAR procedure is applied for the extracted sources, the sources for which photometry has been carried out are removed from the output image of ALLSTAR. Then the ALLSTAR is applied again for the remaining sources. We repeat the ALLSTAR procedure three times to have photometry for all the extracted sources. This is a procedure similar to the one adopted by the GLIMPSE team.
6. The aperture correction is applied to the PSF-fitting results. The aperture correction factors and the PSFs of each band are assumed to be the same among the images. The correction factor is estimated from the median of the differences between the results of the aperture photometry with an aperture of 7.5 and 3.0 pixels applied to all the sources used to construct the “common” PSFs since the absolute calibration was carried out with the aperture photometry with the 7.5 pixel radius for the MIR-S and MIR-L images (Tanabé et al. 2008).

We compare the results of the aperture photometry with those of the PSF-fitting photometry. For the aperture photometry, only steps 1, 2, and 6 above are performed.

3.3. Photometric Calibration

The resultant instrumental signals are converted into physical units using the IRC flux conversion factors (Lorente et al. 2008). Then the calibrated flux densities are converted into magnitudes of the IRC-Vega system using the zero-magnitude flux densities tabulated in Table 1. The differences between the instrumental and the calibrated magnitudes are constant. The zero-magnitude flux densities are estimated for the short- and long-exposure images in each band using the relative spectral response in Onaka et al. (2007). The IRC flux is calibrated against the spectral energy distribution (SED) of $f_\lambda \propto \lambda^{-1}$ or $f_\nu \propto \nu^{-1}$. The color correction factors for objects with different SEDs are tabulated in Lorente et al. (2008). The photometric uncertainty

includes the read-out noises, and the errors in the aperture correction factors and the ADU-to-Jy conversion factors. The values of the read-out noises and the errors of the ADU-to-Jy conversion factors are taken from Tanabé et al. (2008).

3.4. Astrometric Calibration

The attitude control system of the *AKARI* satellite has an absolute position accuracy no better than $5''$ (the requirement was $30''$) and thus the astrometric calibration using other catalogs is necessary to improve the position information of the images. We calculate the coordinate transformation matrix that relates the image pixel coordinates to the sky coordinates by matching the detected point sources in the N3 images with the Two Micron All Sky Survey Point Source Catalog (2MASS-PSC; Skrutskie et al. 2006), and those in the MIR-S and MIR-L images with the *Spitzer* SAGE LMC point-source catalog version 3.1¹³ (SAGE-PSC; Meixner et al. 2006). Sources detected in the MIR-S images are matched with the IRAC [8.0] sources, and those detected in the MIR-L images are matched with the MIPS [24] sources, where the numbers bracketed by [] designate the band of the SAGE catalog; for instance, [3.6] indicates the IRAC 3.6 μm band. The procedure is summarized as follows.

1. The equatorial coordinates (α_i, δ_i) of the 2MASS/SAGE sources in each field are converted to (X_i, Y_i) in the World Coordinate System (WCS).
2. Bright sources in each long-exposure image are extracted.
3. A triangle matching between the 2MASS/SAGE sources in the WCS (X_i, Y_i) and the sources in the pixel coordinates (x_j, y_j) in *AKARI* images is performed with the task XYXYMATCH in IRAF.
4. The transformation matrix is calculated using the pixel coordinates (x_i, y_i) and the equatorial coordinates (α_i, δ_i) of the matched catalog sources with CCMAP in IRAF. The second, third, and fourth orders of polynomials are examined, and then the one with the smallest residuals is adopted.

We use at least five sources that match with the cataloged sources for the calculation. For one S11, five L15, and 74 L24 images, automatic matching with the SAGE catalog is unsuccessful due to the small number of the sources in the images. In such cases, we match the detected point sources with the SAGE-PSC by eye. We use only four sources for the manual matching and thus the positional accuracy in these images could be worse than in others. Point-source matching does not always work for short-exposure images due to the paucity of detected point sources. For 32 S7 and 150 S11 short-exposure images, we could not obtain a sufficient number of sources and the same matrix calculated for the corresponding long-exposure image is applied. The catalog used as the position reference (2MASS-PSC or SAGE-PSC) and the method (e.g., by eye) used for the matching are indicated by the flags for each source (see Section 4).

As described above, the astrometric reference of the present catalog is the 2MASS-PSC and SAGE-PSC. The equatorial coordinates of the 2MASS-PSC are based on the International Celestial Reference System (ICRS), and so is the SAGE-PSC via the 2MASS-PSC. Hence, the equatorial coordinates of the present catalog indirectly refer to the ICRS.

¹³ <http://ssc.spitzer.caltech.edu/spitzermission/observingprograms/legacy/sage/>

3.5. Final Product Generation

3.5.1. Duplicate Source

Each image has overlapping regions of $1/5 \times 10/0$ in its contiguous images. Duplicate sources in the overlapping regions are merged together with the criterion of the spatial proximity of $|\Delta r| \leq 3/0$. The flux density of the one with a better signal-to-noise ratio (S/N) is adopted and the other(s) is discarded. The number of the duplicate sources for each source in each band is denoted by the corresponding code (see Section 4). Note that in most cases the overlapping regions were observed in close pointing opportunities, but in some cases, they were observed in a different season. For a variable source, therefore, the present catalog gives the flux density at a brighter phase.

3.5.2. Merging Short- and Long-exposure Data

The above analysis produces four sets of the result of photometry for a source; two photometry methods (aperture or PSF fitting) and two exposure time data (short or long). Taking account of the errors estimated from the two photometry methods, we adopt the results of the PSF-fitting photometry for the long-exposure data for all the five-band images. For the short-exposure data, we adopt the results of the PSF-fitting photometry for the N3 images and those of the aperture photometry for the S7 and S11 images because reliable PSFs cannot be created for the S7 and S11. The consistency between the long- and short-exposure data is confirmed by the aperture correction procedure in step 6 in Section 3.2 (see also Tanabé et al. 2008). The MIR-L short-exposure data are not adopted in the production of the catalog because of their poor S/N.

To increase the dynamic range, we merge the photometry results of the short- and long-exposure data with a positional tolerance of $3/0$ at the N3, S7, and S11 bands. If a source is detected both in the short- and long-exposure images, we adopt the one with a better S/N and discard the other. The adopted photometry method and the exposure time for a given source are indicated by the corresponding codes (see Section 4).

3.5.3. Band Merging

The photometry results are merged to collect five photometric band data for a given source by the following procedures: (1) merge the N3 list with the S7 list with a positional tolerance of $3/0$ to produce the N3–S7 list, (2) merge the N3–S7 list with the S11 list with a tolerance of $3/0$ to obtain the N3–S7–S11 list, (3) merge the N3–S7–S11 list with the L15 list with a tolerance of $5/0$ to make the N3–S7–S11–L15 list, and (4) merge the N3–S7–S11–L15 list with the L24 list with a tolerance of $5/0$ to obtain the final band-merged list. The matched source is regarded as the same object and the information is merged. The sources not matched remain as independent sources in the list. The number of the matched sources and the distance from the nearest matched source in the merging procedures (1)–(4) are given in the final catalog. If more than one source in the shorter wavelength list are matched in position, the one with the shortest distance is identified as the same source. In such cases, the number of the position-matched sources is given for the source in question, but the source(s) that is not identified as the same source is regarded as a different source and the number of the matched sources is set as zero. Note that the number of the position-matched sources is always given at the longer wavelength band (Table 3). For each of the matched sources, the position of the shortest wavelength band is adopted

as the source position. The band used for the source position determination is indicated by the corresponding code (see Section 4).

3.5.4. Artifact Identification

Similarly to the *Spitzer* IRAC images, the N3 images suffer from the “mux bleed” (signals leaking from bright point sources, making false faint point-like sources every 4 pixels along a row, in which the bright sources are detected) and the “column pulldown” effects (reduction in intensity of the columns in which bright sources are detected). We identify and flag the suspected victims that are located within a belt of ± 5 pixels wide along the rows/columns where bright (saturated) sources are detected. We also flag the sources located near very bright sources, using the proximity radius of 20 pixels for N3, and of 15 pixels for the other bands. The flagged sources should be used with care.

The S7 and S11 images suffer from the noticeable artifacts of bright sources due to the internal reflections in the beam splitter (Arimatsu et al. 2011). We flag the source located at the suspected artifact position that can be estimated accurately from the position of the bright source. No artifacts originating from the beam splitter are present at N3, L15, and L24, and thus no flag for the artifact is given at these bands. The format of the codes is described in Section 4.

3.5.5. Construction of Catalog and Archive

We construct two kinds of catalog, an Archive and a Catalog. The former includes all the detected sources and the latter contains only sources with high reliability.

The Catalog includes only sources that have counterparts in the SAGE-PSC. Although the band profiles of the *AKARI* IRC and the *Spitzer* IRAC/MIPS are not exactly the same, a source detected in the IRC band is likely to be detected in the corresponding IRAC/MIPS band because of their similar sensitivities (Figure 3). We employ the Archive of the SAGE-PSC, which includes more sources than their Catalog, and match the N3 sources with the [3.6] sources, S7, S11, and L15 with [8.0], and L24 with [24], with a positional tolerance of $3/0$. The Archive has more and fainter sources than the Catalog, which may contain potential false detection or sources with larger photometric uncertainties. In total, the Catalog contains 660,286 sources and the Archive has 802,285 sources.

4. THE CATALOG

Table 2 shows the entries for the first 10 sources of the Catalog. The Catalog and the Archive will only be electronically available.¹⁴ The record for a source consists of 554 bytes. Descriptions of each entry of the Catalog and the Archive are summarized in Table 3. The first six entries are common for all the five bands and the rest are the band-specific information. The band-specific entries are bundled together for each band and given in the order of N3, S7, S11, L15, and L24. For the band at which the source is not detected, the band-specific entries are assigned as 99.999 or similar numbers.

The number of the matched sources and the distance from the nearest matched source (Nmat and dis) are given for the longer band. Thus N3 does not have these entries. They are denoted by S7Nmat and S7dis when merging the N3 list with the S7 list. Similarly S11Nmat and S11dis indicate those in

¹⁴ <http://www.ir.isas.jaxa.jp/ASTRO-F/Observation/>

Table 2
Example of the Catalog Record

ID (1)	Name (2)	ID2 (3)	R.A. (4)	Decl. (5)	pos-flag (6)	N3x (7)	N3y (8)	N3mag (9)	N3me (10)	N3me2 (11)	N3chi (12)	N3shrp (13)
56000001	AKARI-LMCC	J050737.46-670810.9	76.906067	−67.136353	3	999.999	999.999	99.999	99.999	99.999	99.999	99.999
56000002	AKARI-LMCC	J050737.51-670831.8	76.906273	−67.142159	3	999.999	999.999	99.999	99.999	99.999	99.999	99.999
56000003	AKARI-LMCC	J050738.23-670640.8	76.909279	−67.111336	3	999.999	999.999	99.999	99.999	99.999	99.999	99.999
56000004	AKARI-LMCC	J050745.94-671413.4	76.941399	−67.237053	3	999.999	999.999	99.999	99.999	99.999	99.999	99.999
56000005	AKARI-LMCC	J050745.96-670811.4	76.941513	−67.136513	3	999.999	999.999	99.999	99.999	99.999	99.999	99.999
56000006	AKARI-LMCC	J050747.82-670821.3	76.949265	−67.139259	3	999.999	999.999	99.999	99.999	99.999	99.999	99.999
56000007	AKARI-LMCC	J050749.56-671211.2	76.956482	−67.203102	3	999.999	999.999	99.999	99.999	99.999	99.999	99.999
56000008	AKARI-LMCC	J050754.92-665746.1	76.978851	−66.962814	3	999.999	999.999	99.999	99.999	99.999	99.999	99.999
56000009	AKARI-LMCC	J050758.73-671218.7	76.994720	−67.205200	3	999.999	999.999	99.999	99.999	99.999	99.999	99.999
56000010	AKARI-LMCC	J050759.70-670035.7	76.998749	−67.009911	3	999.999	999.999	99.999	99.999	99.999	99.999	99.999
...
N3date (14)	N3pid (15)	N3flag (16)	S7Nmat (17)	S7dis (18)	S7x (19)	S7y (20)	S7mag (21)	S7me (22)	S7me2 (23)	S7chi (24)	S7shrp (25)	S7date (26)
9999-99-99T99:99:99	9999999.9	9999999	0	99.99	999.999	999.999	99.999	99.999	99.999	99.999	99.999	9999-99-99T99:99:99
9999-99-99T99:99:99	9999999.9	9999999	0	99.99	999.999	999.999	99.999	99.999	99.999	99.999	99.999	9999-99-99T99:99:99
9999-99-99T99:99:99	9999999.9	9999999	0	99.99	999.999	999.999	99.999	99.999	99.999	99.999	99.999	9999-99-99T99:99:99
9999-99-99T99:99:99	9999999.9	9999999	0	99.99	999.999	999.999	99.999	99.999	99.999	99.999	99.999	9999-99-99T99:99:99
9999-99-99T99:99:99	9999999.9	9999999	0	99.99	999.999	999.999	99.999	99.999	99.999	99.999	99.999	9999-99-99T99:99:99
9999-99-99T99:99:99	9999999.9	9999999	0	99.99	999.999	999.999	99.999	99.999	99.999	99.999	99.999	9999-99-99T99:99:99
9999-99-99T99:99:99	9999999.9	9999999	0	99.99	999.999	999.999	99.999	99.999	99.999	99.999	99.999	9999-99-99T99:99:99
9999-99-99T99:99:99	9999999.9	9999999	0	99.99	999.999	999.999	99.999	99.999	99.999	99.999	99.999	9999-99-99T99:99:99
9999-99-99T99:99:99	9999999.9	9999999	0	99.99	999.999	999.999	99.999	99.999	99.999	99.999	99.999	9999-99-99T99:99:99
9999-99-99T99:99:99	9999999.9	9999999	0	99.99	999.999	999.999	99.999	99.999	99.999	99.999	99.999	9999-99-99T99:99:99
9999-99-99T99:99:99	9999999.9	9999999	0	99.99	999.999	999.999	99.999	99.999	99.999	99.999	99.999	9999-99-99T99:99:99
...
S7pid (27)	S7flag (28)	S11Nmat (29)	S11dis (30)	S11x (31)	S11y (32)	S11mag (33)	S11me (34)	S11me2 (35)	S11chi (36)	S11shrp (37)	S11date (38)	S11pid (39)
9999999.9	9999999	0	99.99	999.999	999.999	99.999	99.999	99.999	99.999	99.999	9999-99-99T99:99:99	9999999.9
9999999.9	9999999	0	99.99	999.999	999.999	99.999	99.999	99.999	99.999	99.999	9999-99-99T99:99:99	9999999.9
9999999.9	9999999	0	99.99	999.999	999.999	99.999	99.999	99.999	99.999	99.999	9999-99-99T99:99:99	9999999.9
9999999.9	9999999	0	99.99	999.999	999.999	99.999	99.999	99.999	99.999	99.999	9999-99-99T99:99:99	9999999.9
9999999.9	9999999	0	99.99	999.999	999.999	99.999	99.999	99.999	99.999	99.999	9999-99-99T99:99:99	9999999.9
9999999.9	9999999	0	99.99	999.999	999.999	99.999	99.999	99.999	99.999	99.999	9999-99-99T99:99:99	9999999.9
9999999.9	9999999	0	99.99	999.999	999.999	99.999	99.999	99.999	99.999	99.999	9999-99-99T99:99:99	9999999.9
9999999.9	9999999	0	99.99	999.999	999.999	99.999	99.999	99.999	99.999	99.999	9999-99-99T99:99:99	9999999.9
9999999.9	9999999	0	99.99	999.999	999.999	99.999	99.999	99.999	99.999	99.999	9999-99-99T99:99:99	9999999.9
9999999.9	9999999	0	99.99	999.999	999.999	99.999	99.999	99.999	99.999	99.999	9999-99-99T99:99:99	9999999.9
...

Table 2
(Continued)

S11flag (40)	L15Nmat (41)	L15dis (42)	L15x (43)	L15y (44)	L15mag (45)	L15me (46)	L15me2 (47)	L15chi (48)	L15shrp (49)	L15date (50)	L15pid (51)	L15flag (52)
9999999	0	99.99	206.406	18.121	10.662	0.207	0.209	0.075	0.052	2007-05-28T11:25:56	2213033.1	1100000
9999999	0	99.99	197.784	16.530	9.297	0.072	0.073	0.107	−0.085	2007-05-28T11:25:56	2213033.1	1100000
9999999	0	99.99	243.089	27.315	10.074	0.143	0.144	0.114	−0.189	2007-05-28T11:25:56	2213033.1	1100000
9999999	0	99.99	53.203	8.753	10.766	0.251	0.253	0.100	0.036	2007-05-28T11:25:56	2213033.1	1100000
9999999	0	99.99	202.099	38.444	8.544	0.052	0.053	0.175	−0.077	2007-05-28T11:25:56	2213033.1	1100000
9999999	0	99.99	197.140	42.089	10.436	0.197	0.199	0.104	−0.161	2007-05-28T11:25:56	2213033.1	1100000
9999999	0	99.99	101.755	27.399	10.834	0.255	0.257	0.090	−0.152	2007-05-28T11:25:56	2213033.1	1100000
9999999	0	99.99	237.879	28.323	8.954	0.062	0.063	0.131	0.128	2007-06-02T23:59:44	2213035.1	1100000
9999999	0	99.99	94.249	48.691	9.652	0.097	0.098	0.108	0.015	2007-05-28T11:25:56	2213033.1	1100000
9999999	0	99.99	165.741	32.491	10.831	0.236	0.239	0.067	0.063	2007-06-02T23:59:44	2213035.1	1100000
...
L24Nmat (53)	L24dis (54)	L24x (55)	L24y (56)	L24mag (57)	L24me (58)	L24me2 (59)	L24chi (60)	L24shrp (61)	L24date (62)	L24pid (63)	L24flag (64)	
0	99.99	999.999	999.999	99.999	99.999	99.999	99.999	99.999	9999-99-99T99:99:99	9999999.9	9999999	
1	0.27	193.778	11.330	9.226	0.225	0.229	0.154	−0.260	2007-05-28T11:27:37	2213033.1	1100000	
0	99.99	999.999	999.999	99.999	99.999	99.999	99.999	99.999	9999-99-99T99:99:99	9999999.9	9999999	
0	99.99	999.999	999.999	99.999	99.999	99.999	99.999	99.999	9999-99-99T99:99:99	9999999.9	9999999	
1	1.23	197.763	33.093	7.008	0.035	0.038	0.161	−0.020	2007-05-28T11:27:37	2213033.1	1100000	
0	99.99	999.999	999.999	99.999	99.999	99.999	99.999	99.999	9999-99-99T99:99:99	9999999.9	9999999	
0	99.99	999.999	999.999	99.999	99.999	99.999	99.999	99.999	9999-99-99T99:99:99	9999999.9	9999999	
1	1.10	233.541	22.642	7.041	0.029	0.034	0.096	−0.061	2007-06-03T00:01:26	2213035.1	1100000	
1	0.36	90.170	43.412	8.157	0.078	0.081	0.122	0.125	2007-05-28T11:27:37	2213033.1	1100000	
0	99.99	999.999	999.999	99.999	99.999	99.999	99.999	99.999	9999-99-99T99:99:99	9999999.9	9999999	
...	

Table 3
Catalog Content

Item	Format	Record Position (Byte)					Content
Common record							
ID1	A8	1:8					Source ID1: 56***** for Catalog and 51***** for Archive
Cname	A10	10:19					AKARI-LMCC for Catalog and AKARI-LMCA for Archive
ID2	A19	21:39					Source ID2 in Jhhmmss.ss-ddmmss.s
R.A.	F10.6	41:50					Right ascension (J2000.0) in degree
Decl.	F10.6	52:61					Declination (J2000.0) in degree
eq-flag	A1	63:63					Band at which the position is derived
Band specific							
		N3	S7	S11	L15	L24	
x	F7.3	65:71	165:171	265:271	365:371	465:471	Pixel X-coordinate
y	F7.3	73:79	173:179	273:279	373:379	473:479	Pixel Y-coordinate
Mag	F6.3	81:86	181:186	281:286	381:386	481:486	Magnitude in the Vega system uncorrected for extinction
me1	F6.3	88:93	188:193	288:293	388:393	488:493	Photometric uncertainty from ALLSTAR
me2	F6.3	95:100	195:200	295:300	395:400	495:500	Total photometric uncertainty ^a
χ	F7.3	102:108	202:208	302:308	402:408	502:508	PSF fit parameter ^b
Sharpness	F7.3	110:116	210:216	310:316	410:416	510:516	PSF fit parameter ^c
Date	A19	118:136	218:236	318:336	418:436	518:536	Observation date in UT
PID	A9	138:146	238:246	338:346	438:446	538:546	Pointing ID
Flag	A7	148:154	248:254	348:354	448:454	548:554	Seven-digit code for the object (see the text and Table 4)
Nmatch	I2	...	156:157	256:257	356:357	456:457	Number of matched sources (see the text for details)
Distance	F5.2	...	159:163	259:263	359:363	459:463	Distance from the nearest matched source in arcsec (see the text for details)

Notes.^a Including errors in the aperture correction, read-out noise, and conversion factor.^b The parameter χ increases with the difference in shape between the source and the PSF profile. The value 99.999 is assigned when the aperture photometry is employed.^c A positive (negative) sharpness indicates that the source is more (less) extended than the PSF-profile, suggesting that the source may be a galaxy, an unresolved multi-star system, a cosmic ray, or image defect. The value 99.999 is assigned when the aperture photometry is employed.**Table 4**
Description of Flags

Flag	Description
Exposure	0: short; 1: long
Photometry	0: aperture photometry; 1: PSF-fitting photometry
Multiple	Number of the nearby sources
Mux bleed	1: contamination by mux bleed; only for N3
Column pulldown	1: contaminated by column pulldown; only for N3
Artifact	1: contaminated by artifact; only for S7 and S11

merging the N3–S7 list with the S11 list, L15Nmat and L15dis in merging the N3–S7–S11 list with the L15 list, and L24Nmat and L24dis in merging the N3–S7–S11–L15 list with the L24 list.

The flag code consists of seven characters, one for each flag: “exposure,” “photometry,” “saturation,” “mux bleed,” “column pulldown,” “artifact,” and “multiple” flags, respectively. The description of the flags is summarized in Table 4. Of these, the “saturation,” “mux bleed,” “column pulldown,” and “artifact” flags are set to 1 if the source has a possibility of being affected by these phenomena (see Section 3.5.4). The “exposure” flag denotes photometry either from the short (0) or the long (1) exposure data, the “photometry” flag denotes the photometry method employed, 0 for the aperture photometry and 1 for the fit photometry (see Section 3.5.2), and the “multiple” flag provides the number of nearby sources (see Section 3.5.1). The code is given for all the bands, but “mux bleed” and “column pulldown” are only given at N3, and “artifact” is assigned only at S7 and S11 (see Section 3.5.4).

Table 5
Internal Dispersion of Photometry and Astrometry

Band	σ (mag)	σ ($''$)	S/N	N_{source}
N3	0.091	0.607	≥ 30	10805
S7	0.071	0.413	≥ 20	3500
S11	0.058	0.405	≥ 20	1314
L15	0.069	0.962	≥ 20	497
L24	0.063	1.031	≥ 20	455

5. GENERAL CHARACTERISTICS OF THE CATALOG*5.1. Accuracy of Photometry and Astrometry**5.1.1. Photometric Accuracy*

The photometric accuracy of the present data set is estimated from the internal consistency of measured flux of the sources in the overlapping regions. Table 5 summarizes the median of the dispersions in the magnitude of the sources observed in more than one pointing observations. The dispersion at N3 (~ 0.09 mag) is larger than those at S7 and S11 (~ 0.06 – 0.07). Bright sources must include a large number of variable stars. Thus the present dispersions are affected both by the photometric uncertainties and the variability of the sources and indicate upper limits of the photometric uncertainties. Part of the large dispersion at N3 may come from the variability, although a study of the variables based on the SAGE data does not indicate a strong spectral dependence of the variability from 3 to 8 μm (Vijh et al. 2009). It could also be attributed to the variable PSF of the N3 images due to jitters in the *AKARI* satellite pointing.

Table 6
Astrometric Accuracy

Catalog	Offset		Standard Deviation			Accuracy
	$\Delta\alpha$	$\Delta\delta$	$\Delta\alpha$	$\Delta\delta$	r	
2MASS-PSC	$-0''.064$	$0''.056$	$0''.220$	$0''.307$	$0''.393$	$\sim 0''.07^a$
SAGE-PSC	$-0''.058$	$0''.057$	$0''.293$	$0''.421$	$0''.509$	$\sim 0''.3^b$

Notes.^a Skrutskie et al. (2006).^b Sewilo et al. (2009).

5.1.2. Astrometric Accuracy

The median of the dispersions in the positions of the sources detected at multiple pointing observations is summarized in Table 5. The dispersion at shorter wavelengths is smaller than that at longer wavelengths except for N3 (Section 3.5.3). The dispersion at N3 is slightly worse than those at S7 and S11. This may originate in the distorted PSF at N3, which comes from aberrations of the *AKARI* telescope on orbit (Kaneda et al. 2007) or tracking errors in the attitude control system since the exposure time of N3 is by three times longer than the MIR band data. The sources detected at multiple bands adopt the position determined in the shortest wavelength band despite the slightly worse dispersion at N3.

We compare the positions in the present catalog with those in the 2MASS-PSC and the SAGE-PSC. The systematic offsets and the standard deviations between the corresponding positions are listed in Table 6. The deviation from the SAGE-PSC is $\sim 0''.5$, which is slightly larger than that from the 2MASS-PSC of $\sim 0''.4$. This is attributable to the difference in the astrometric accuracy between the SAGE-PSC of $\sim 0''.3$ (Sewilo et al. 2009) and the 2MASS-PSC of $\sim 0''.07$ (Skrutskie et al. 2006). Taking account of these facts, we estimate the uncertainty in the position of the present catalog as $\sim 0''.4$. This value is in agreement with that of the internal consistency. The offsets from the 2MASS-PSC and the SAGE-PSC are consistent with each other. The systematic offset of the present catalog from the ICRS is estimated to be less than $0''.1$.

5.2. Detection Limit and Completeness

5.2.1. Limiting Magnitude

The distributions of the photometric uncertainty versus magnitude for the sources in the Archive and the Catalog are shown in Figure 2 for each band; the dashed horizontal lines indicate an S/N of 10. The 10σ limiting magnitude is the faintest magnitude at which the mode of the photometric uncertainties of the sources in the Catalog becomes 0.11 mag. The 10σ limiting magnitudes are 16.8, 13.4, 11.5, 9.9, and 8.5 mag at N3, S7, S11, L15, and L24, respectively, as listed in Table 7. Figure 2 indicates the presence of two branches in the sources in the Archive except for N3: one for which σ goes below 0.1 mag at the brightest end and the other in which σ stays above 0.1 mag. The latter branch disappears in the plot of the Catalog sources (left), suggesting that they do not have counterparts in the SAGE catalog. We will discuss this issue in Section 5.3.

Figure 3 is a diagrammatic representation of the 5σ limiting magnitudes of the present survey, the *Spitzer* SAGE survey, and the IRSF/SIRIUS near-infrared survey. The 5σ limiting magnitudes of the present survey are calculated from the 10σ limiting magnitudes given in Table 7. We estimate the 10σ limiting magnitudes for the SAGE survey by the same procedure

Table 7
 10σ Limiting Magnitude and 90% Completeness Limit

Band	10σ Limiting Magnitude	90% Completeness Limit		
		High (mag) ^a	Medium (mag) ^a	Blank (mag) ^a
N3	17.9	13.46 ± 0.13	14.58 ± 0.08	15.66 ± 0.08
S7	13.8	10.73 ± 0.41	13.40 ± 0.87	14.06 ± 0.18
S11	12.4	9.12 ± 0.73	12.62 ± 0.08	12.84 ± 0.05
L15	9.9	7.70 ± 1.21	10.68 ± 0.29	11.02 ± 0.13
L24	8.6	5.88 ± 1.12	9.32 ± 0.25	9.50 ± 0.07

Note. ^a High, medium, and blank correspond to the sky-background level (see the text).

as described above, then calculate the 5σ limiting magnitudes. Figure 3 indicates that the limiting magnitudes of the present survey are slightly worse than those of the SAGE survey, while the S11 and L15 bands fill the gap of the SAGE data with comparable sensitivities. Examples of the *Infrared Space Observatory* (ISO) SWS spectra of stars of known distance (the distances are taken from Crosas & Menten 1997 for IRC +10216 and Perryman et al. 1997 for others) are also plotted after scaling their flux densities at the distance of the LMC. Here, the distance modulus of the LMC is assumed to be 18.5 mag. The figure indicates that all red giants above the tip of the first red giant branch (TRGB) and some fraction of Herbig Ae/Be stars in the LMC can be detected at shorter than 11 μm in the present survey.

5.2.2. Completeness Limit

The completeness limit is estimated by adding artificial sources of various magnitudes and measuring the detection probability of the sources. Artificial sources with the shape of the PSF model are added by an IDL software. We adopt 90% probability as the completeness limit. To estimate the completeness limits with different sky-background levels, the following three cases are investigated in each band: (1) “high”: images with the highest sky-background level, (2) “medium”: images with the median of the sky-background level of all images, and (3) “blank”: images with the lowest sky-background level. For each level, five images without large masked areas or artifacts are selected and artificial sources are embedded.

The averages and standard deviations of the 90% completeness limits estimated from five images at each level are listed in Table 7. In all bands, the 90% completeness limits with the “medium” level are comparable to those with the “blank” level and those with the “high” level are by ~ 3 mag shallower than those with the other two. The “high” sky-background level is higher by three standard deviations than the median of the sky-background levels of all images in each band. The fraction of the images with the “high” sky-background level is only 1%–2%. More than 90% of the images have a sky-background level within two standard deviations from the median of the sky-background level of all the images at each band. Therefore, the typical completeness limits are comparable to those with the “medium” level. The 90% completeness limits with the “medium” level are 14.6, 13.4, 12.6, 10.7, and 9.3 mag at N3, S7, S11, L15, and L24, respectively. They are roughly comparable with the 10σ limiting magnitudes except at N3, where it is by ~ 2 mag shallower than the 10σ limiting magnitudes. This can be attributed to confusion due to the relatively large number of sources at N3.

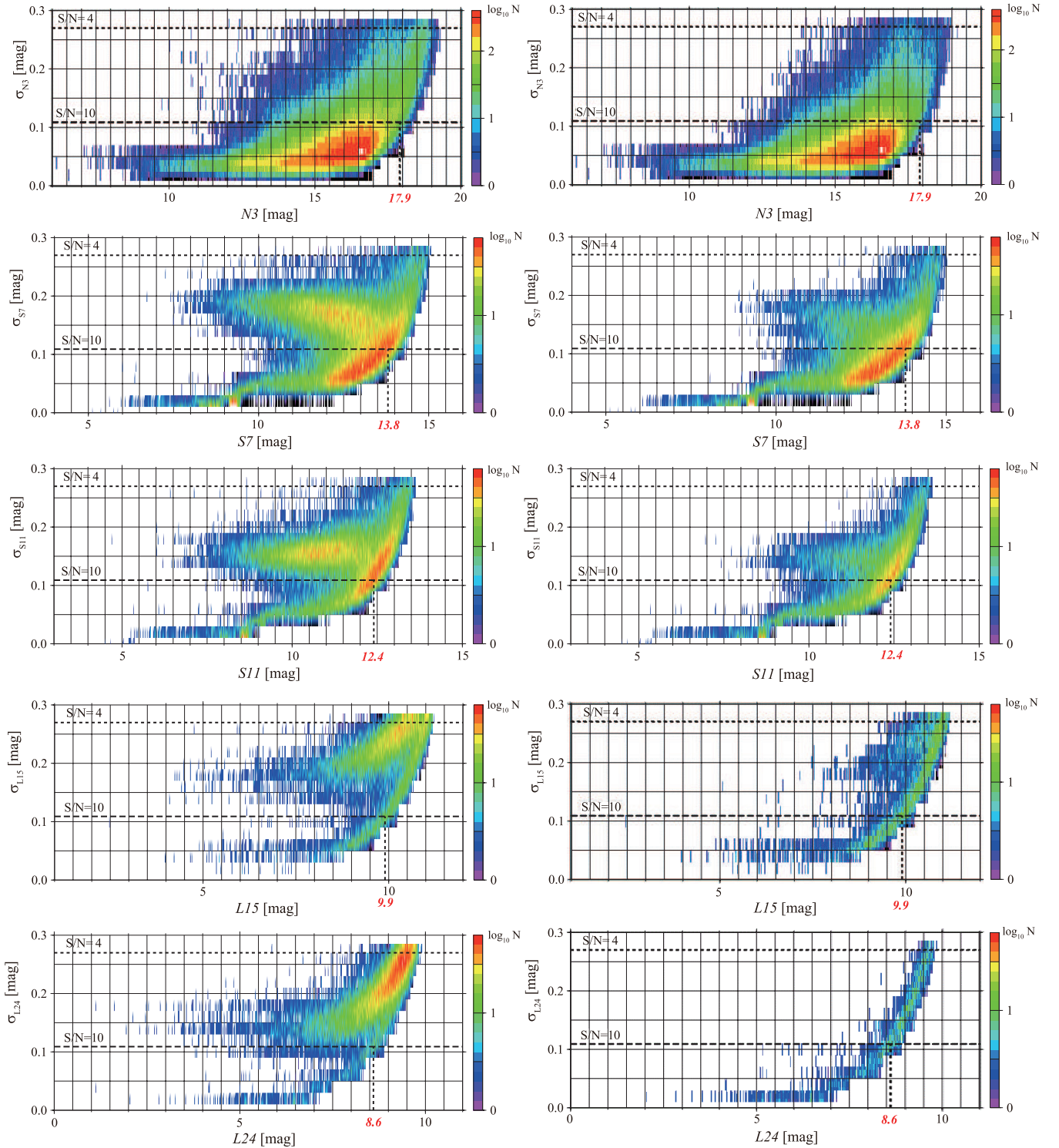


Figure 2. Photometric uncertainties as a function of magnitude for the Archive sources (left) and the Catalog sources (right) at N3, S7, S11, L15, and L24 from top to bottom. The horizontal dashed lines indicate the S/N levels of 2, 4, and 10, and the vertical dotted lines show the 10σ limiting magnitudes.

(A color version of this figure is available in the online journal.)

5.3. Comparison with Spitzer SAGE Point-source Catalog

As described in Section 3.5.5, we construct two kinds of catalog: the Archive, which includes all the detected sources, and the Catalog, which includes sources that have a counterpart(s) in the closest band of the SAGE-PSC. Therefore, the ratio between the number of the sources in the Catalog and that in the Archive in a band is the fraction of the *AKARI* sources that

have a counterpart(s) in the SAGE-PSC. The ratios are 85.0%, 56.8%, 43.4%, 25.1%, and 4.8% at N3, S7, S11, L15, and L24, respectively. Since a large fraction of the area of the *AKARI* survey is covered by the SAGE survey and the sensitivities are comparable (see Section 5.2.1), the ratios are unexpectedly small except for N3.

The spatial distributions of the Archive and the Catalog sources in S7, S11, L15, and L24 images around bright

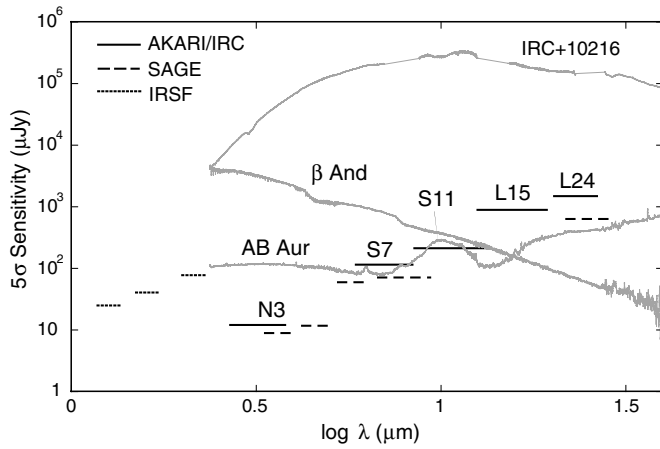


Figure 3. Graphic representation of the 5σ detection limits of the *AKARI* LMC survey (solid lines). For a comparison, the 5σ detection limits of the *Spitzer* SAGE survey and the IRSF/SIRIUS survey are shown by the dashed and dotted lines, respectively. The length of the bars indicates the FWHM of the bandpass. *ISO* SWS spectra (Sloan et al. 2003) of three galactic stars are also plotted after scaling their fluxes at the distance of the LMC as examples of a Herbig Ae/Be star (AB Aur), a red giant with luminosities below the TRGB (β And), and a dusty red giant (IRC +10216).

nebulousity are shown in Figure 4 to investigate the difference in more detail. It indicates that the sources only in the Archive are concentrated along bright nebulousity. Figure 5 shows the

Table 8
Band Merging Results^a

Band	Archive		Catalog		Matching Band
	N_{all}^b	N_{match}^c	N_{all}^b	N_{match}^c	
S7	141617	101425	89610	85791	N3
S11	97226	67254	48525	43355	S7
L15	42974	27141	16712	12868	S11
L24	52266	23062	6856	5545	L15

Notes.

^a For merging strategy, see the text.

^b Total number of sources.

^c Number of sources with a counterpart in the neighboring shorter wavelength band.

relationship between the sharpness and the magnitude for the Archive and Catalog sources at N3, S7, S11, L15, and L24. The sharpness parameter indicates the size of the source compared to the PSF. A positive (negative) sharpness value indicates that the source is more (less) extended than the PSF. The Archive sources at S7, S11, L15, and L24 show distributions around unity, suggesting that they are more extended than point-like sources. These distributions are not seen in the Catalog sources.

Table 8 summarizes the number of the sources with a counterpart in the neighboring shorter wavelength band as well as the number of all the sources in the Archive and the Catalog.

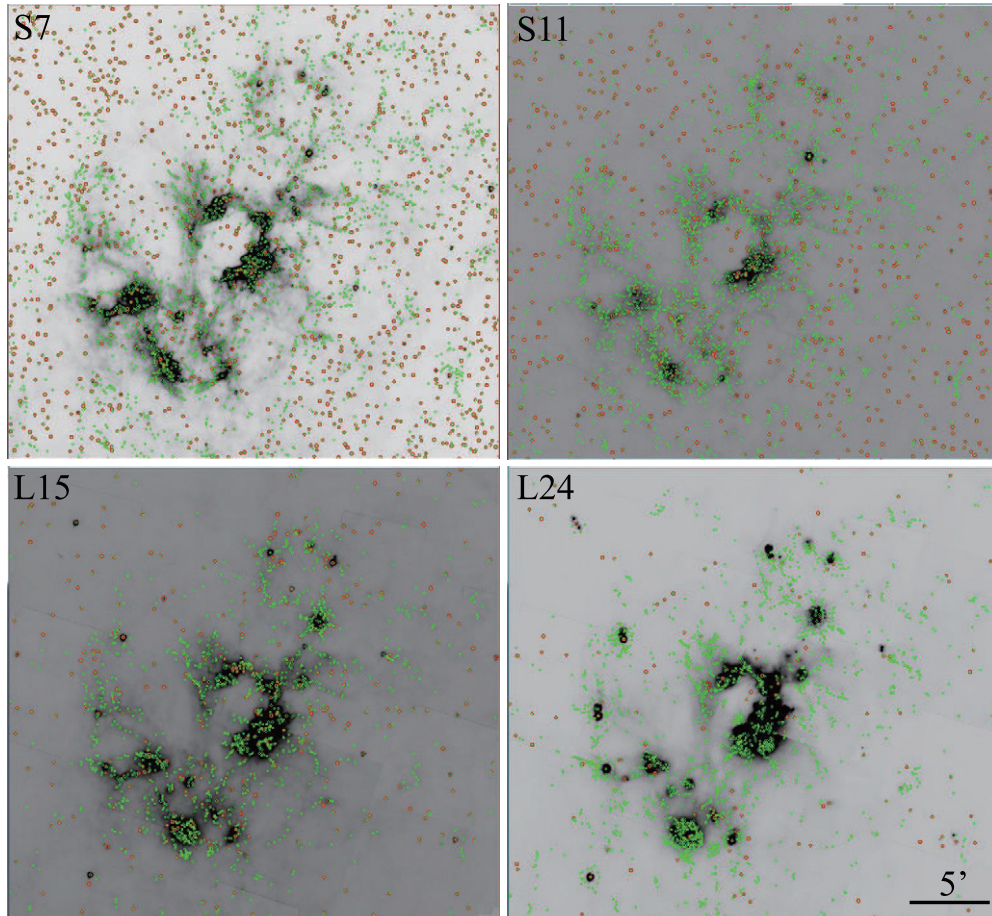


Figure 4. Spatial distributions of Archive (green) and Catalog sources (red) on the S7 (top left), S11 (top right), L15 (bottom left), and L24 (bottom right) images around bright nebulae. The image size is $30' \times 30'$ and the central position of the image is ($5^{\text{h}}22^{\text{m}}08^{\text{s}}$, $-67^{\text{d}}56^{\text{m}}12^{\text{s}}$).

(A color version of this figure is available in the online journal.)

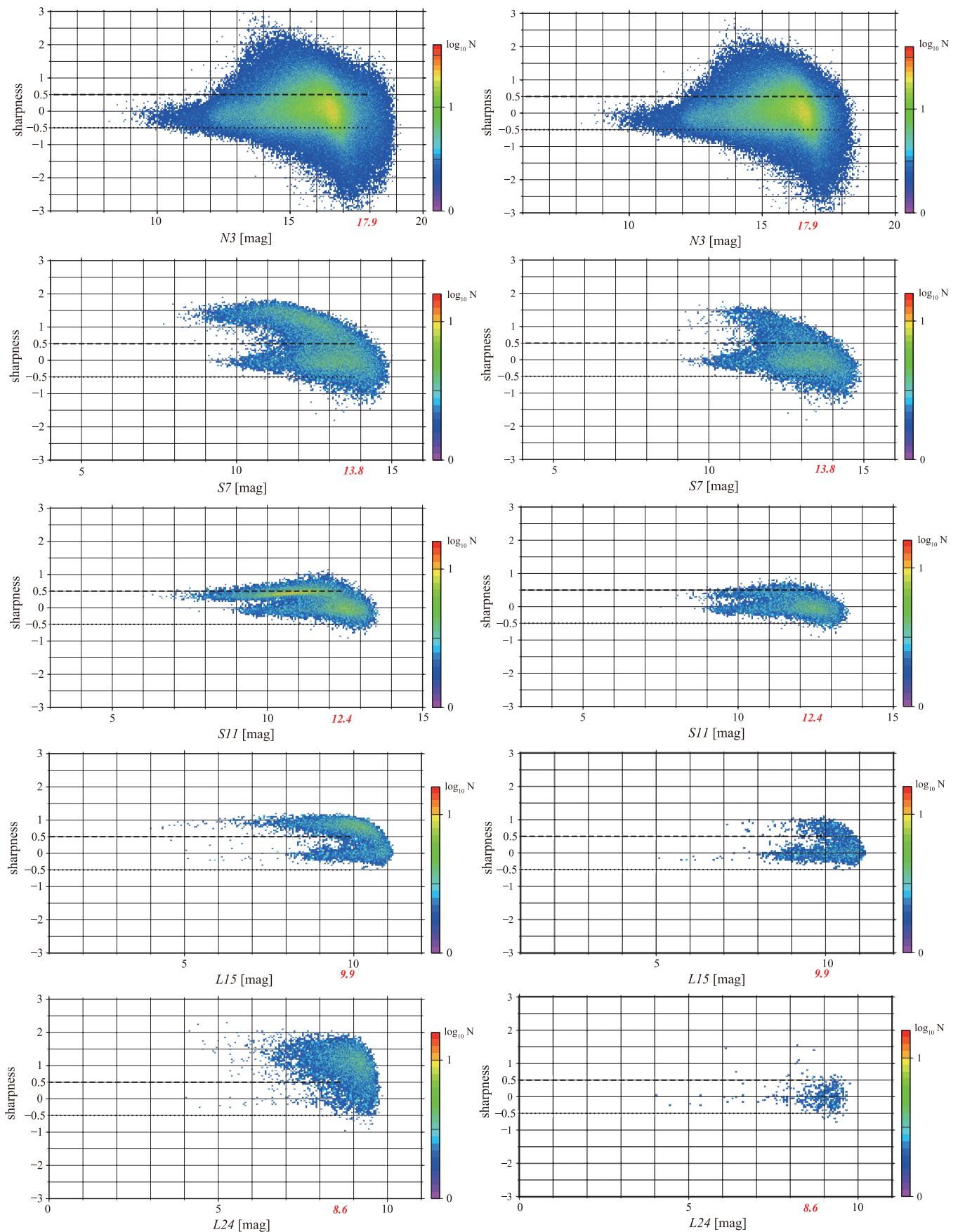


Figure 5. Sharpness vs. magnitude. The left figure shows the Archive sources and the right indicates the Catalog sources at N3, S7, S11, L15, and L24 from top to bottom. The numbers in red indicate the 10σ limiting magnitudes.

(A color version of this figure is available in the online journal.)

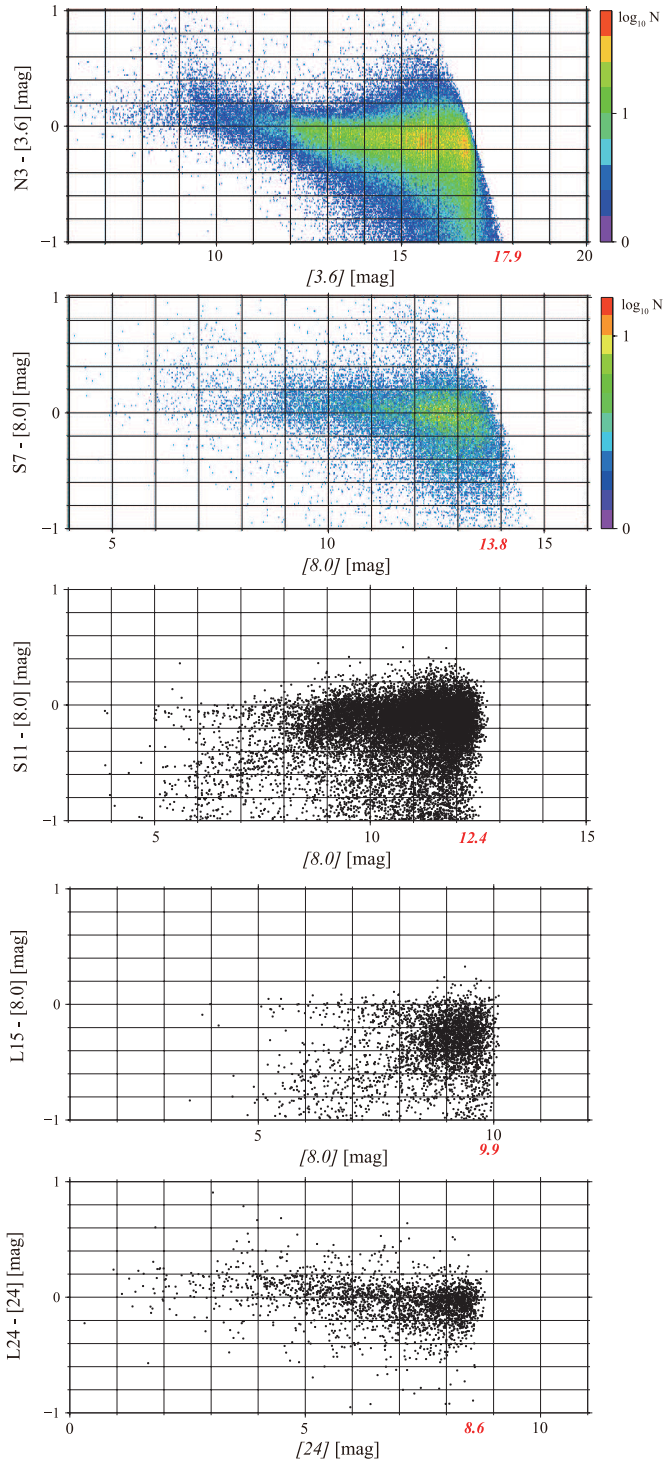


Figure 6. Comparison of the magnitudes of the *AKARI* catalog and SAGE-PSC. Residual magnitudes of the sources matched between the *AKARI* catalog and SAGE-PSC are shown as a function of magnitude at N3 (with SAGE [3.6]), S7, S11, L15 (with [8.0]), and L24 (with [24]) from top to bottom. The numbers in red indicate the 10σ limiting magnitudes of the *AKARI* catalog.

(A color version of this figure is available in the online journal.)

The S7 sources are matched with the N3 sources, S11 with S7, L15 with S11, and L24 with L15. A significant fraction of the Archive sources have a counterpart in the neighboring shortest wavelength band for S7, S11, L15, and L24. These facts suggest that the Archive sources are real, but that they are slightly

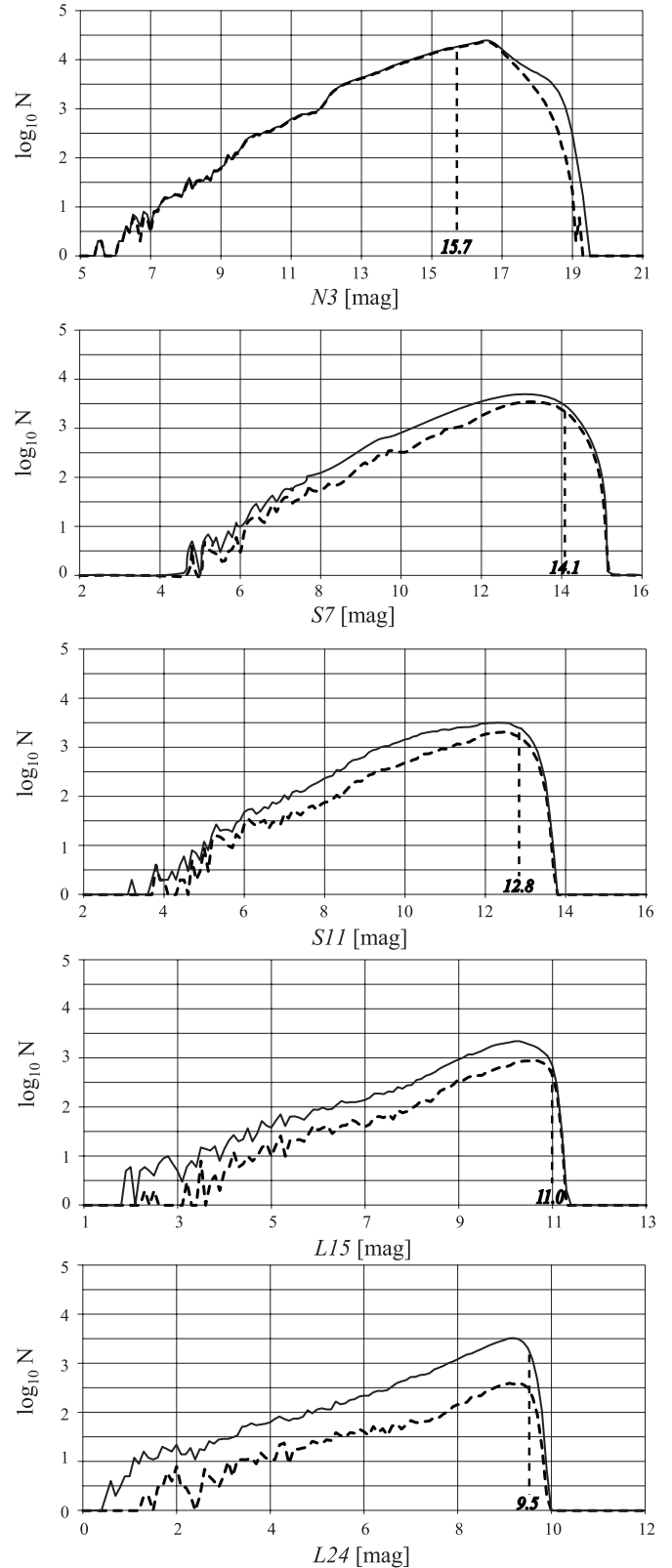


Figure 7. Luminosity functions. From top to bottom those at N3, S7, S11, L15, and L24 are shown in 0.1 mag bins. The solid and dashed lines show the Archive and Catalog sources, respectively. The numbers in italic and the vertical dashed lines indicate the 90% completeness limits in “blank” regions.

extended for the beam of *Spitzer* and thus are not included in the SAGE-PSC as a true point source. Figure 2 indicates that the Archive sources excluded in the SAGE catalog have larger flux uncertainties than those in the Catalog except for N3. The larger

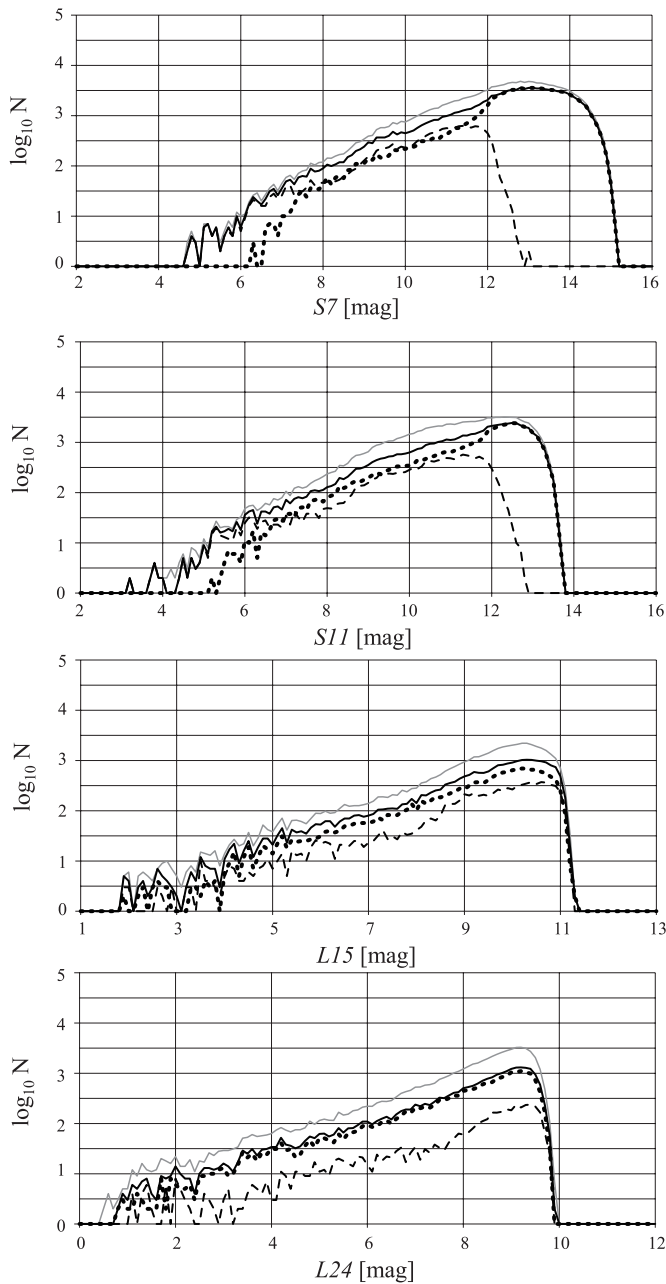


Figure 8. Luminosity functions of the Archive sources. Those at S7, S11, L15, and L24 are shown from top to bottom. The gray lines indicate all Archive sources, the black solid lines those with a counterpart in N3 sources, and the dashed and dotted lines those with a counterpart of N3 brighter and fainter than 12 mag, respectively.

uncertainties may be attributable to the nebulosity with which the sources are associated as suggested by the larger sharpness. The associated nebulosity is appreciably seen in the MIR and increases the background fluctuation. The imperfect match with the PSF for slightly extended sources could also increase the uncertainties.

Figure 6 shows the distributions of the difference between the N3, S7, and L24 magnitudes and the [3.6], [8.0], and [24] in the SAGE-PSC for the Catalog sources. Although systematic differences are present, which can be attributed to the difference in the relative spectral responses, all the bands show fairly linear correlations, confirming the consistency in the photometric results between the two data sets.

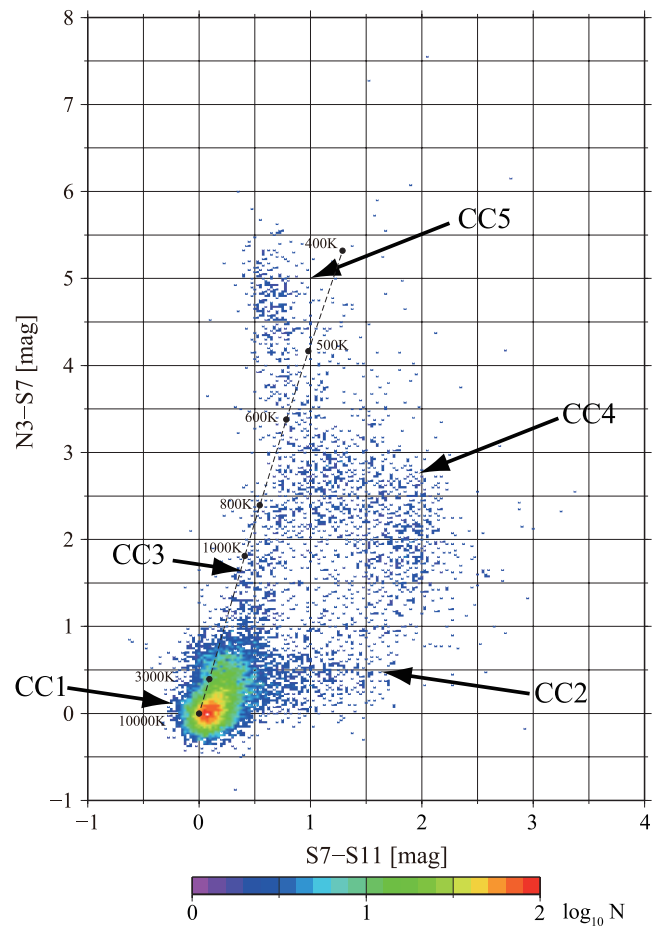


Figure 9. Color-color diagram of $[N3] - [S7]$ vs. $[S7] - [S11]$. The Archive sources with $S/Ns \geq 10$ are shown. Each color is binned by 0.025 mag and the number density levels are shown in a logarithmic scale. The dashed line is a locus of the colors for blackbodies from temperatures of 400 to 10,000K. Noticeable features are labeled as CC1–CC5 (see the text).

(A color version of this figure is available in the online journal.)

6. PROPERTIES OF THE SOURCES IN THE CATALOG

In this section, we discuss the following properties of the sources in the present catalog: (1) luminosity functions (LFs), (2) a color-color diagram (CCD), and (3) a color-magnitude diagram (CMD).

6.1. Luminosity Functions

The LFs for the five bands are shown in Figure 7. For the magnitudes brighter than 2–4 mag, all of the LFs start to fall rapidly due to the saturation. In the N3 LF, there is a stepwise increase around 12 mag, which corresponds to the flux of TRGB (Ita et al. 2008). To investigate the populations of the sources that contribute to the LFs at L15 and L24, we also plot the Archive sources that have N3 counterparts brighter and fainter than 12 mag separately by the dotted and dashed lines in Figure 8. In the LFs of S7 and S11, there are no apparent differences depending on the brightness of the N3 counterparts brighter than 11.5 mag, but the sources fainter than 12 mag at N3 become dominant for those fainter than 11.5 mag. In the LFs of L15 and L24, the sources fainter than 12 mag at N3 are dominant irrespective of the magnitude. At the present sensitivities, TRGB without dust shells cannot be detected at L15 and L24 (Figure 3). Therefore, those that contribute to the LFs of L15 and L24 are likely to be dusty AGB stars whose

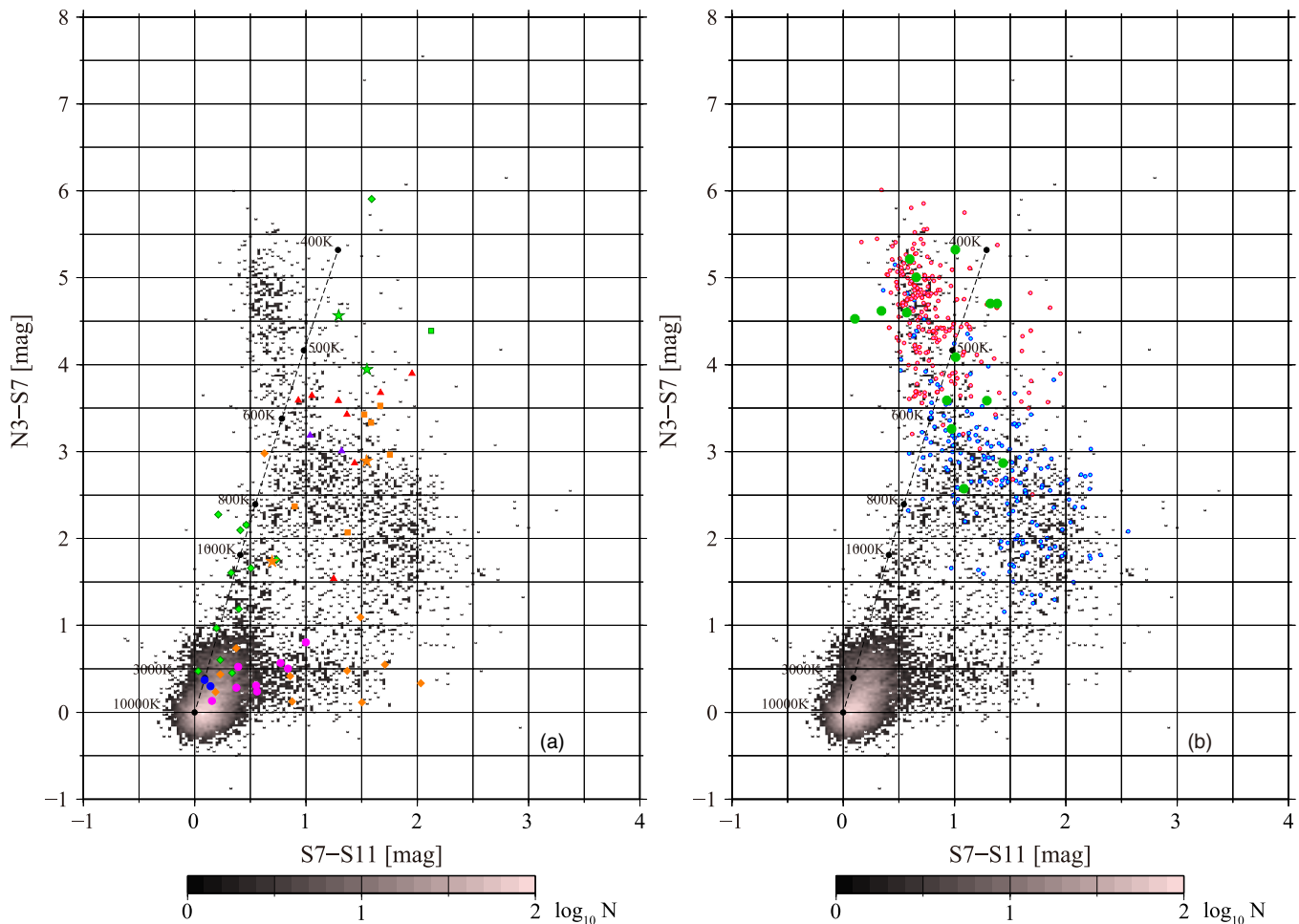


Figure 10. Color-color diagram of $[N3] - [S7]$ vs. $[S7] - [S11]$. The Archive sources with $S/Ns \geq 10$ are plotted in a gray scale together with the sources classified in Woods et al. (2011) in (a) and with the YSO and background galaxy candidates selected by Gruendl & Chu (2009) in (b). In (a), the blue and purple circles indicate naked stars and red supergiants, the orange and green diamonds represent O-rich and C-rich AGB stars, the orange and green squares show O-rich and C-rich post-AGB stars, the orange and green stars indicate O-rich and C-rich planetary nebulae, and the purple and red triangles show H II regions and YSOs, respectively. In (b), the blue and red circles show background galaxy and YSO candidates, respectively. The green circles indicate YSOs with the water ice absorption at $3 \mu m$ (Shimonishi et al. 2010; Shimonishi 2012).

(A color version of this figure is available in the online journal.)

$N3$ is significantly attenuated. Other types of objects, such as background galaxies, are also supposed to be present.

6.2. Color-Color Diagram

Ita et al. (2008) discuss the characteristics of the CCD of $[N3] - [S11]$ versus $[S11] - [L15]$ using the preliminary *AKARI* LMC catalog, where the brackets $[\]$ indicate the magnitude at the band in question. Based on the same catalog, Siudek et al. (2012) present the distributions of about 2000 sources that are detected at all the IRC five bands and have information of the object type on CCDs and CMDs of various combinations. They also discuss the classification of objects using the Support Vector Machine algorithm. These investigations demonstrate the importance of the bands $S11$ and $L15$ in the classification, which are unique to *AKARI*. Ita et al. (2008) suggest that even the $N3$ data contain different information from the IRAC $3.6 \mu m$ band. The short cutoff wavelength of the $N3$ band is $2.7 \mu m$ (Onaka et al. 2007), much shorter than that of the IRAC $3.6 \mu m$ band (Fazio et al. 2004) of $3.185 \mu m$. The $N3$ band is more sensitive to the absorption at $3 \mu m$ either of water ice seen in young stellar objects (YSOs) or of C_2H_2 and HCN in carbon stars. Although it contains interesting information, $L15$ may not have

a sufficient depth to probe low-mass YSOs (Figure 3 and see below). Therefore we investigate the CCD of $[N3] - [S7]$ versus $[S7] - [S11]$, a combination of the most sensitive three bands, here in some detail.

Figure 9 shows the $[S7] - [S11]$ versus $[N3] - [S7]$ CCD for the Archive sources with $S/Ns \geq 10$ at $N3$, $S7$, and $S11$. The sample contains 16446 sources. In the CCD, there are five noticeable features, which are labeled as CC1–CC5. Group CC1 forms a clump around $([S7] - [S11], [N3] - [S7]) \sim (0, 0)$. Groups CC2 and CC3 constitute sequences extending from CC1 to redder regions; CC2 is a horizontally stretching feature to $([S7] - [S11], [N3] - [S7]) \sim (3, 1)$, whereas CC3 is a vertical sequence to $\sim (1, 2.5)$. CC4 forms a diffuse concentration around $([S7] - [S11], [N3] - [S7]) \sim (1.5, 2.5)$ and CC5 is a sequence vertically extending from CC3 further to $([S7] - [S11], [N3] - [S7]) \sim (0.7, 5.5)$.

Woods et al. (2011) classify 197 point sources in the LMC based on SAGE-Spec observations with the Infrared Spectrograph (IRS) on board *Spitzer* (Houck et al. 2004). With a positional tolerance of $10''.0$, 67 sources in Woods et al. (2011) are found to match with the Archive sources. Figure 10(a) highlights these matched sources by the large symbols. Two naked

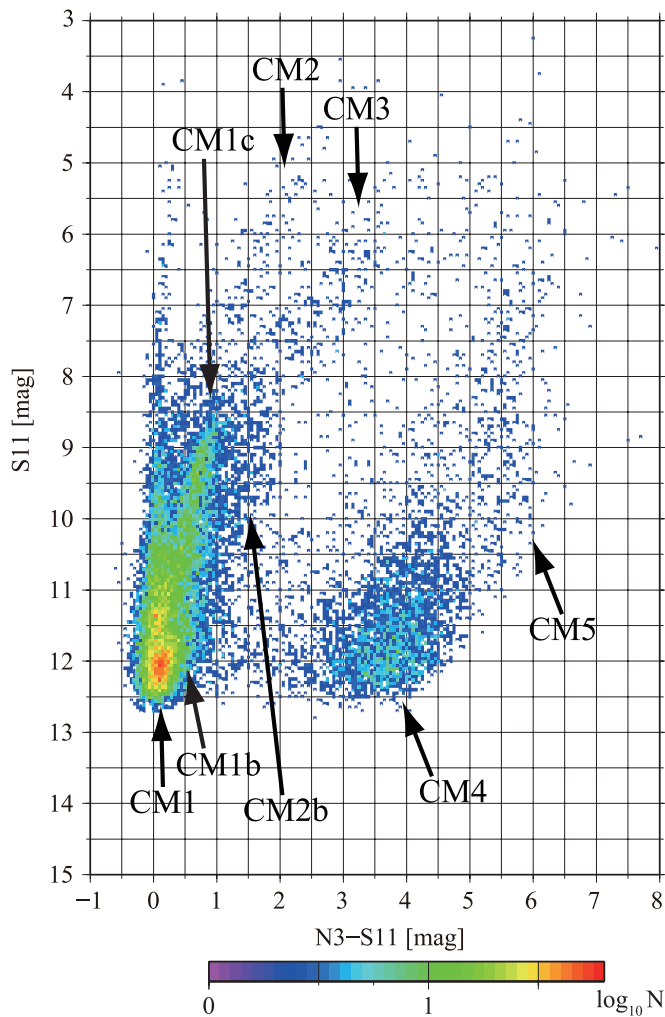


Figure 11. Color-magnitude diagram of $[S11]$ vs. $[N3] - [S11]$. The Archive sources with $S/Ns \geq 10$ are plotted. Each data point is binned by 0.05 mag and the number density levels are shown in a logarithmic scale. Noticeable features are labels as CM1–CM5 (see the text).

(A color version of this figure is available in the online journal.)

stars matched (blue circles) are located at CC1 and red supergiants (purple circles) are distributed over CC1 and CC2. O-rich AGB stars (orange diamonds) are located at CC2, while C-rich AGB stars (green diamonds) are located at CC3 and CC5. O-rich post-AGB stars (orange squares) and O-rich planetary nebulae (orange stars) are distributed in the CC4 region. Only one C-rich post-AGB star and one C-rich planetary nebulae are matched with the Archive sources and they are located at CC5 as indicated by the green square and star, respectively. Two H II regions are matched (purple triangles), which are seen in the CC4–CC5 regions. No background galaxies in their sample are matched with the Archive. YSOs (red triangles) are located at CC5. It should be noted that these YSOs are most likely massive ones because of the detection limit of the IRS (Woods et al. 2011). Sources in CC4 and CC5 also include post-AGB stars and planetary nebulae.

In Figure 10(b), background galaxy and YSO candidates selected by Gruendl & Chu (2009) are plotted on the same CCD together with the Archive sources. Gruendl & Chu (2009) select the candidates based on the analysis using the images and photometry of the *Spitzer* SAGE survey as well as other surveys from optical to NIR wavelengths. With a positional tolerance

of $3''$, 379 YSO and 239 background galaxy candidates are matched with the Archive sources. Figure 10(b) shows that CC5 selectively overlaps with YSO candidates, while background galaxies and other YSOs are distributed around the CC4 region. It also indicates a clear separation between YSO and background galaxy candidates around $[N3] - [S7] \sim 3.5$, which is roughly consistent with the boundary between CC4 and CC5. The color $[N3] - [S7]$ becomes very red for YSOs because of the water ice absorption at $3 \mu\text{m}$ (Shimonishi et al. 2008), whereas $[S7] - [S11]$ stays blue due to the silicate absorption (Woods et al. 2011). To confirm the effect of the water ice absorption, the YSOs that show the absorption (Shimonishi et al. 2010; Shimonishi 2012) are also plotted by the green circles in Figure 10(b). Eleven of the 14 YSOs are located in the CC5 region, while the rest three are in the CC4 region, supporting the above interpretation. The S7 band efficiently probes the unidentified infrared bands at 6.2 and $7.7 \mu\text{m}$ (Onaka et al. 2009), which also accounts partly for the redness of $[N3] - [S7]$. Therefore, the color $[N3] - [S7]$ is efficient to distinguish YSOs from dusty AGB stars. Further observations of the objects in the CC5 region would be interesting to study their nature and investigate the applicability of this color diagnosis. Background galaxies can have very red $[S7] - [S11]$ color, but their $[N3] - [S7]$ color may not be very red because stellar components contribute to N3. Post-AGB stars or planetary nebulae are also suggested to be distributed in the CC4 region (Siudek et al. 2012).

In summary, the features CC1–CC5 in the $[S7] - [S11]$ versus $[N3] - [S7]$ CCD correspond to the following objects.

- CC1: naked stars;
- CC2: dusty O-rich stars;
- CC3: dusty C-rich stars;
- CC4: YSOs and background galaxy candidates, and post-AGB and planetary nebulae;
- CC5: YSO candidates with water ice absorption.

These classifications are also confirmed by the investigation of known objects toward the LMC (Siudek et al. 2012).

Figure 9 shows the distributions of the sources similar to those seen in the $[S11] - [L15]$ versus $[N3] - [S11]$ CCD based on the previous version of the *AKARI* LMC catalog (Ita et al. 2008) except for CC5, which is not seen in their diagram. Their classifications of each feature are in agreement with the present results. The absence of CC5 in the $[S11] - [L15]$ versus $[N3] - [S11]$ CCD may suggest that the present sensitivity of *L15* is not sufficient to detect most YSOs in the LMC.

6.3. Color-Magnitude Diagram

Classification based on the CMDs has been extensively discussed for the SAGE-SPC data (e.g., Blum et al. 2006; Whitney et al. 2008). Ita et al. (2008) present CMDs of several combinations of the imaging bands based on the previous version of the *AKARI* catalog. Here we only briefly discuss a CMD that shows a well-separated distribution of various objects to confirm the previous results. Figure 11 shows the $[N3] - [S11]$ versus $[S11]$ CMD for the Archive sources with $S/Ns \geq 10$ at N3, S7, and S11. Comparison with the five components CC1–CC5 in the CCD indicates

1. CC1 sources form a vertically stretching feature along $[N3] - [S11] \sim 0$ (CM1) and two separate branches in $0 < [N3] - [S11] < 1.5$ (CM1b and CM1c);

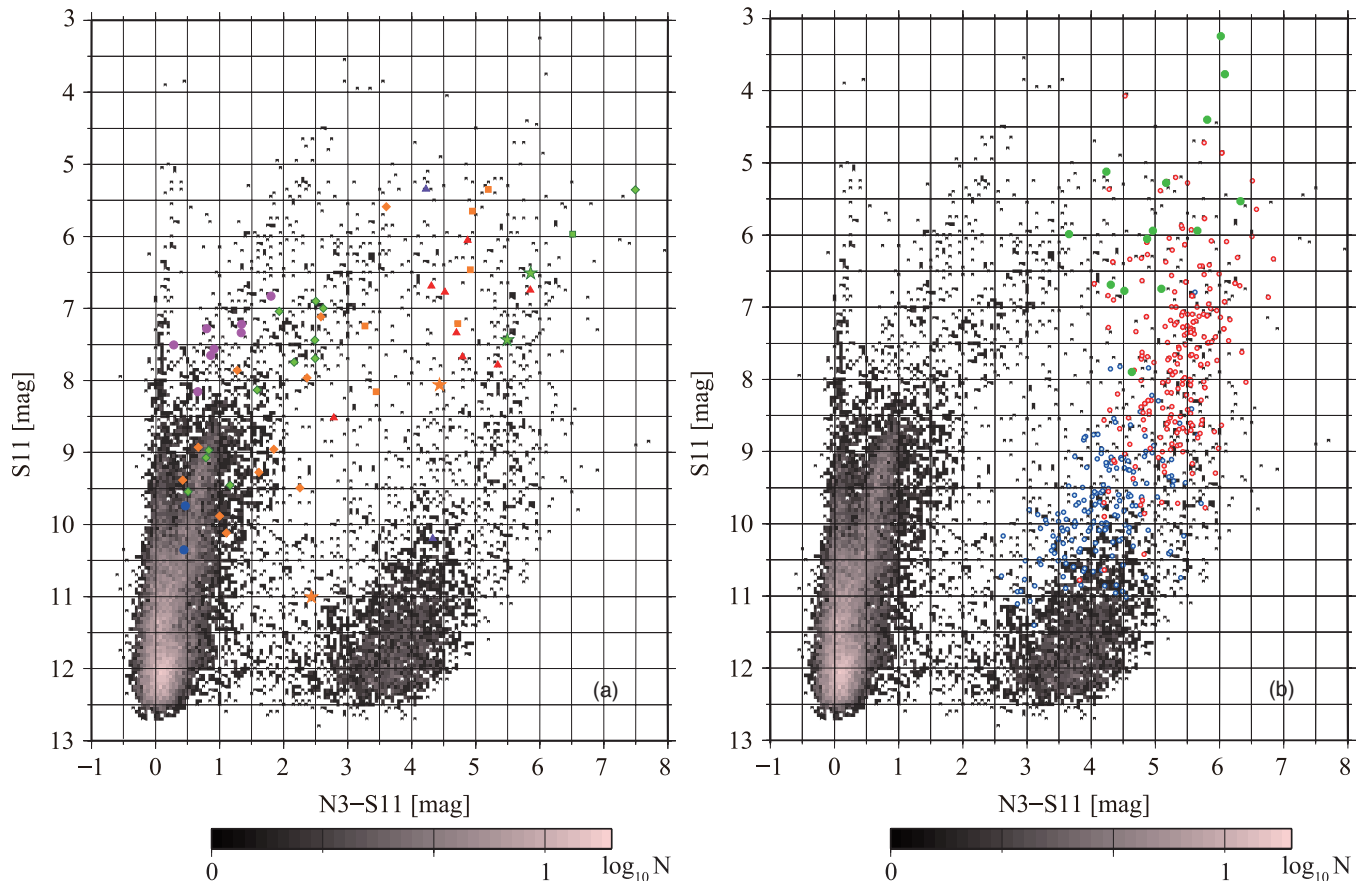


Figure 12. Color-magnitude diagram of $[S11]$ vs. $[N3] - [S11]$. The Archive sources with $S/Ns \geq 10$ are plotted in a gray scale together with the sources classified in Woods et al. (2011) in (a) and YSO and background galaxy candidates by Gruendl & Chu (2009) in (b). The symbols are the same as in Figures 10(a) and (b). (A color version of this figure is available in the online journal.)

2. CC2 sources form a finger-like feature (CM2) and a clump around $([N3] - [S11], [S11]) \sim (1.5, 9.5)$ (CM2b);
3. CC3 sources form a finger-like structure (CM3);
4. CC4 sources form a clump (CM4);
5. CC5 sources are distributed to the redder region (CM5).

The sequence CM1b corresponds to a bristle-shape feature, which Ita et al. (2008) attribute to the broad emission feature of aluminum oxide grains around $11.4 \mu\text{m}$ (e.g., Onaka et al. 1989).

Comparison with their CMD suggests that the distributions of dusty C-rich AGB stars are located at the position of CM3 and those of optical carbon stars correspond to the sequence CM1c ($([N3] - [S11], [S11]) \sim (0.5, 10.5)$ to $(1.0, 8.5)$). Other features are also basically seen in the CMD of Ita et al. (2008), confirming the previous results by the improved catalog.

We find a new feature CM2b in Figure 11. The sources of CM2b are found to correspond to CC2 in the CCD (Figure 9), which we assign to dusty O-rich stars (see Figure 10(a)). According to stellar evolution models (e.g., Herwig 2000; Straniero et al. 2006; Karakas & Lattanzio 2007), the third dredge-up enhances the abundance of carbon relative to oxygen for stars with $\geq 2 M_{\odot}$, which leads to the formation of C-rich stars (Lebzelter et al. 2009). For stars with $\geq 4 M_{\odot}$, the hot bottom burning decreases the abundance of carbon, which then prevents the formation of C-rich stars (García-Hernández et al. 2006). These suggest that AGB stars with an intermediate mass ($\sim 2-4 M_{\odot}$) have a high probability of evolving to C-rich stars, and low-mass ($\leq 2 M_{\odot}$) and high-mass ($\sim 4-8 M_{\odot}$)

AGB stars are likely to evolve to O-rich stars. Thus theoretical predictions suggest that CM2 and CM2b in Figure 11 correspond to high-mass and low-mass O-rich stars, respectively. Note that both mass limits depend on the metallicity (Boothroyd et al. 1993) and thus the location of CM2b may differ in other galaxies.

In Figure 12(a), 67 Archive sources classified in Woods et al. (2011) are highlighted as in Figure 10(a). The locations of each category source are in agreement with the above discussion. Red supergiants (purple circles) are found to be concentrated on CM2. Post-AGB stars (squares) and planetary nebulae (stars) are distributed over a wide area in the CMD. YSOs with the ice absorption are located at $[S11] < 7$ mag, while those with the emission features are distributed at $[S11] > 6.5$ mag.

In Figure 12(b), background galaxy and YSO candidates (Gruendl & Chu 2009) are plotted on the CMD together with the Archive sources. Figure 12 indicates that YSO candidates are located around CM5 and background galaxy candidates are distributed over the brighter side of CM4. Gruendl & Chu (2009) exclude faint and red sources from the initial YSO candidates with a criterion of $[8.0] > 14 - ([4.5] - [8.0])$ to avoid contamination from background galaxies. Faint CM4 sources are likely to be excluded in this selection. Therefore the entire CM4 population can be attributed to background galaxies. These assignments of the features in the CMD are well in agreement with those made in the CCD. The locations of the YSOs with the $3 \mu\text{m}$ water ice absorption (green circles) reported in Shimonishi et al. (2010) and Shimonishi (2012) are in agreement with those classified by Woods et al. (2011) in Figure 12(a).

7. SUMMARY

We present the *AKARI* LMC Point-Source Catalog, which covers a core 10 deg^2 area of the LMC with five photometric bands: N3 ($3.2 \mu\text{m}$), S7 ($7 \mu\text{m}$), S11 ($11 \mu\text{m}$), L15 ($15 \mu\text{m}$), and L24 ($24 \mu\text{m}$). The 10σ limiting magnitudes are 17.9, 13.8, 12.4, 9.9, and 8.6 mag at N3, S7, S11, L15, and L24, respectively. They are comparable to those of the *Spitzer* SAGE survey and the S11 and L15 data smoothly fill the gap between the IRAC and MIPS bands. The photometric accuracy is estimated to be better than 0.1 mag at N3 and 0.06–0.07 mag in the other bands. The astrometric accuracy is $0''.3$ at N3, S7, and S11, and $1''.0$ at L15 and L24.

We provide a source Catalog and an Archive: The Archive contains all the detected sources, while the Catalog only includes sources that have a counterpart in the *Spitzer* SAGE point-source catalog. The Archive contains about 650,000, 140,000, 97,000, 43,000, and 52,000 sources at 3.2, 7, 11, 15, and $24 \mu\text{m}$, respectively.

Based on the present catalog, we discuss the LFs at five bands, a CCD, and a CMD of the N3, S7, and S11 data for the sources toward the LMC. Several noticeable features are recognized in the CCD and CMD, which can be attributed to naked stars, dusty C-rich and O-rich AGB stars, background galaxies and YSOs. They are distributed at distinct locations on the diagrams, indicating that the present data provide useful information on the classification of the sources toward the LMC.

This work is based on observations with *AKARI*, a JAXA project with the participation of ESA. The authors thank all the members of the *AKARI* project and the members of the LMC survey for their continuous help and encouragement. They are grateful to F. Egusa for her contribution to the IRC data reduction pipeline. They also thank the *Spitzer* SAGE team for their help. This work is supported in part by Grants-in-Aid from the Japan Society for the Promotion of Science (JSPS).

Facility: AKARI

REFERENCES

- Alves, D. R. 2004, *New Astron. Rev.*, **48**, 659
 Arimatsu, K., Onaka, T., Sakon, I., et al. 2011, *PASP*, **123**, 981
 Benjamin, R. A., Churchwell, E., Babler, B. L., et al. 2003, *PASP*, **115**, 953
 Blum, R. D., Mould, J. R., Olsen, K. A., et al. 2006, *AJ*, **132**, 2034
 Boothroyd, A. I., Sackmann, I. J., & Ahern, S. C. 1993, *ApJ*, **416**, 762
 Crosas, M., & Menten, K. M. 1997, *ApJ*, **483**, 913
 Egan, M. P., Price, S. D., Kraemer, K. E., et al. 2003, Air Force Research Laboratory Technical Report, Vol. AFRL-VS-TR-2003-1589
 Egan, M. P., Van Dyk, S. F., & Price, S. D. 2001, *AJ*, **122**, 1844
 Fazio, G. G., Hora, J. L., Allen, L. E., et al. 2004, *ApJS*, **154**, 10
 García-Hernández, D. A., García-Lario, P., Plez, B., Manchado, A., & D'Antona, F. 2006, in IAU Symp. 234, Planetary Nebulae in Our Galaxy and Beyond, ed. M. J. Barlow & R. H. Méndez (Cambridge: Cambridge Univ. Press), **87**
 Gruendl, R., & Chu, Y. 2009, *ApJS*, **184**, 172
 Herwig, F. 2000, *A&A*, **360**, 952
 Houck, J. R., Roellig, T. L., van Cleve, J., et al. 2004, *ApJS*, **154**, 18
 Ishihara, D., Onaka, T., Kataza, H., et al. 2010, *A&A*, **514**, A1
 Ita, Y., Onaka, T., Kato, D., et al. 2008, *PASJ*, **60**, S435
 Ita, Y., Tanabé, T., Matsunaga, N., et al. 2007, *PASJ*, **59**, S437
 Kaneda, H., Kim, W., Onaka, T., et al. 2007, *PASJ*, **59**, S423
 Karakas, A., & Lattanzio, J. 2007, *PASA*, **24**, 103
 Kato, D., Nagashima, C., Nagayama, T., et al. 2007, *PASJ*, **59**, 615
 Kawada, M., Baba, H., Barthel, P. D., et al. 2007, *PASJ*, **59**, S389
 Kemper, F., Woods, P. M., Antoniou, V., et al. 2010, *PASP*, **892**, 683
 Lebzelter, T., Lederer, M. T., Cristallo, S., Straniero, O., & Hinkle, K. H. 2009, in IAU Symp. 256, The Magellanic System: Stars, Gas, and Galaxies, ed. J. Th. van Loon & J. M. Oliveira (Cambridge: Cambridge Univ. Press), **397**
 Lorente, R., Onaka, T., Ita, Y., et al. 2008, *AKARI IRC Data User's Manual*, ver. 1.4, <http://www.ir.isas.jaxa.jp/AKARI/Observation/>
 Luck, R. E., Moffett, T. J., Barnes, T. G., III, & Geren, W. P. 1998, *AJ*, **115**, 605
 Meixner, M., Galliano, F., Hony, S., et al. 2010, *A&A*, **518**, L71
 Meixner, M., Gordon, K. D., Indebetouw, R., et al. 2006, *AJ*, **132**, 2288
 Murakami, H., Baba, H., Barthel, P., et al. 2007, *PASJ*, **59**, S369
 Ohya, Y., Onaka, T., Matsuhara, H., et al. 2007, *PASJ*, **59**, S411
 Onaka, T., de Jong, T., & Willems, F. J. 1989, *A&A*, **218**, 169
 Onaka, T., Kaneda, H., Sakon, I., & Matsumoto, H. 2009, in ASP Conf. Ser. 414, Proc. Cosmic Dust—Near and Far, ed. Th. Henning, E. Grün, & J. Steinacker (San Francisco, CA: ASP), **227**
 Onaka, T., Matsuhara, H., Wada, T., et al. 2007, *PASJ*, **59**, S401
 Perryman, M. A. C., Lindegren, L., Kovalevsky, J., et al. 1997, *A&A*, **323**, L49
 Rieke, G. H., Young, E. T., Engelbracht, C. W., et al. 2004, *ApJS*, **154**, 25
 Sewilo, M., Meixner, M., Whitney, B., et al. 2009, The SAGE Data Products Description, <http://ssc.spitzer.caltech.edu/spitzermission/observingprograms/legacy/sage/>
 Shimonishi, T. 2012, PhD thesis, Univ. Tokyo
 Shimonishi, T., Onaka, T., Kato, D., et al. 2008, *ApJ*, **686**, L99
 Shimonishi, T., Onaka, T., Kato, D., et al. 2010, *A&A*, **514**, A12
 Shimonishi, T., Onaka, T., Kato, D., et al. 2012, *AJ*, submitted
 Siudek, M., Pollo, A., Takeuchi, T. T., et al. 2012, Earth, Planets, Space, in press
 Skrutskie, M. F., Cutri, R. M., Stiening, R., et al. 2006, *AJ*, **131**, 1163
 Sloan, G. C., Kathleen, E., Kraemer, K. E., Price, S. D., & Shipman, R. F. 2003, *ApJS*, **147**, 379
 Stetson, P. B. 1987, *PASP*, **99**, 191
 Straniero, O., Gallino, R., & Cristallo, S. 2006, *Nucl. Phys. A*, **777**, 311
 Tanabé, T., Sakon, I., Cohen, M., et al. 2008, *PASJ*, **60**, S375
 van Loon, J. T., Oliverira, J. M., Gordon, K. D., et al. 2010, *AJ*, **139**, 68
 Vihj, U. P., Meixner, M., Babler, B., et al. 2009, *AJ*, **137**, 3139
 Werner, M. W., Roellig, T. L., Low, F. J., et al. 2004, *ApJS*, **154**, 1
 Whitney, B. A., Sewilo, M., Indebetouw, R., et al. 2008, *AJ*, **136**, 18
 Woods, P. M., Oliveira, J. M., Kemper, F., et al. 2011, *MNRAS*, **411**, 1597
 Yamamura, I., Makiuti, S., Ikeda, N., et al. 2010, VizieR On-line Data Catalog: II/298
 Zaritsky, D., Harris, J., Thompson, I. B., & Grebel, E. K. 2004, *AJ*, **128**, 1606